

Chapter 6

3D field data applications

In this chapter, I present different applications of regularized joint image-domain inversion—developed in chapter 3—to three-dimensional time-lapse ocean-bottom-cable (OBC) data sets. Recall that in chapter 5, I described some important preprocessing steps required for regularized joint image-domain inversion and showed that the method improves time-lapse amplitude information in a two-dimensional marine streamer time-lapse data set. The data studied in this chapter are preprocessed subsets of full-azimuth OBC data sets acquired as part of BP’s Valhall Life of Field Seismic (LoFS) reservoir-monitoring project.

Valhall is a giant oil field located in the southern part of the Norwegian sector of the North Sea. The reservoir in this field is made up of high-porosity, low-permeability Cretaceous chalk at a depth of approximately 2,400 m—at the crest of the structure (Munns, 1985). The reservoir thickness varies between 10 and 60 m (Munns, 1985). This field is located at a water depth of about 60 m, and has been on production since 1982 (Barkved et al., 2003).

The Valhall LoFS project utilizes a permanent recording system of ocean bottom cables to provide continuous monitoring of changes in reservoir and overburden properties caused by hydrocarbon production and water injection in the field. Changes in fluid content, together with the associated changes in the pressure and stress regimes,

result in large changes in the acoustic properties of the rocks within and around the reservoir. In addition, because of the high porosity of the reservoir rocks, hydrocarbon production and water injection cause compaction and overburden subsidence in the field (van Gestel et al., 2008). Therefore, there are strong time-lapse seismic responses associated with hydrocarbon production and water injection in the field.

The Valhall field has been studied extensively. Today, there is a wide range of published work on different aspects of hydrocarbon exploration, on the field development and production history, and on various aspects of the LoFS reservoir monitoring project. For example, Munns (1985) discusses the geology and stratigraphy of the Valhall field in detail; Ali and Alcock (1994) and Barkved et al. (2003) discuss the production history and development plans for the field; Barkved (2004) discusses the permanent seismic acquisition array and the key objectives of the LoFS reservoir monitoring project; Kommedal et al. (2007) and van Gestel et al. (2008) discuss aspects of the seismic data acquisition, processing, and analysis; Hatchell et al. (2005) and van Gestel et al. (2011) discuss aspects of the seismic data interpretation and integration with other reservoir data; and Barkved et al. (2010) discuss the impact of robust velocity model building—by full waveform inversion—on static and dynamic imaging in the field.

For this study, I use available subsets of the original LoFS seismic data sets. These subsets cover the Southern flank of the Valhall structure, far away from the gas clouds located above the crest of the Valhall structure. Figure 6.1 shows the location of gas cloud within the baseline velocity model—obtained by full waveform inversion (Sirgue et al., 2010). Note the location of the target area for this study relative to the gas clouds (Figure 6.1). These gas clouds present some challenges to seismic imaging, and consequently to seismic monitoring. As noted in previous chapters, conventional imaging does not fully account for illumination distortions, which in this case are caused by the relatively low velocity of the gas clouds. Therefore, regularized joint inversion—which compensates for such distortions—will potentially have more positive impact in monitoring the reservoir under the gas clouds. However, the data required for such a study are currently not available at Stanford.

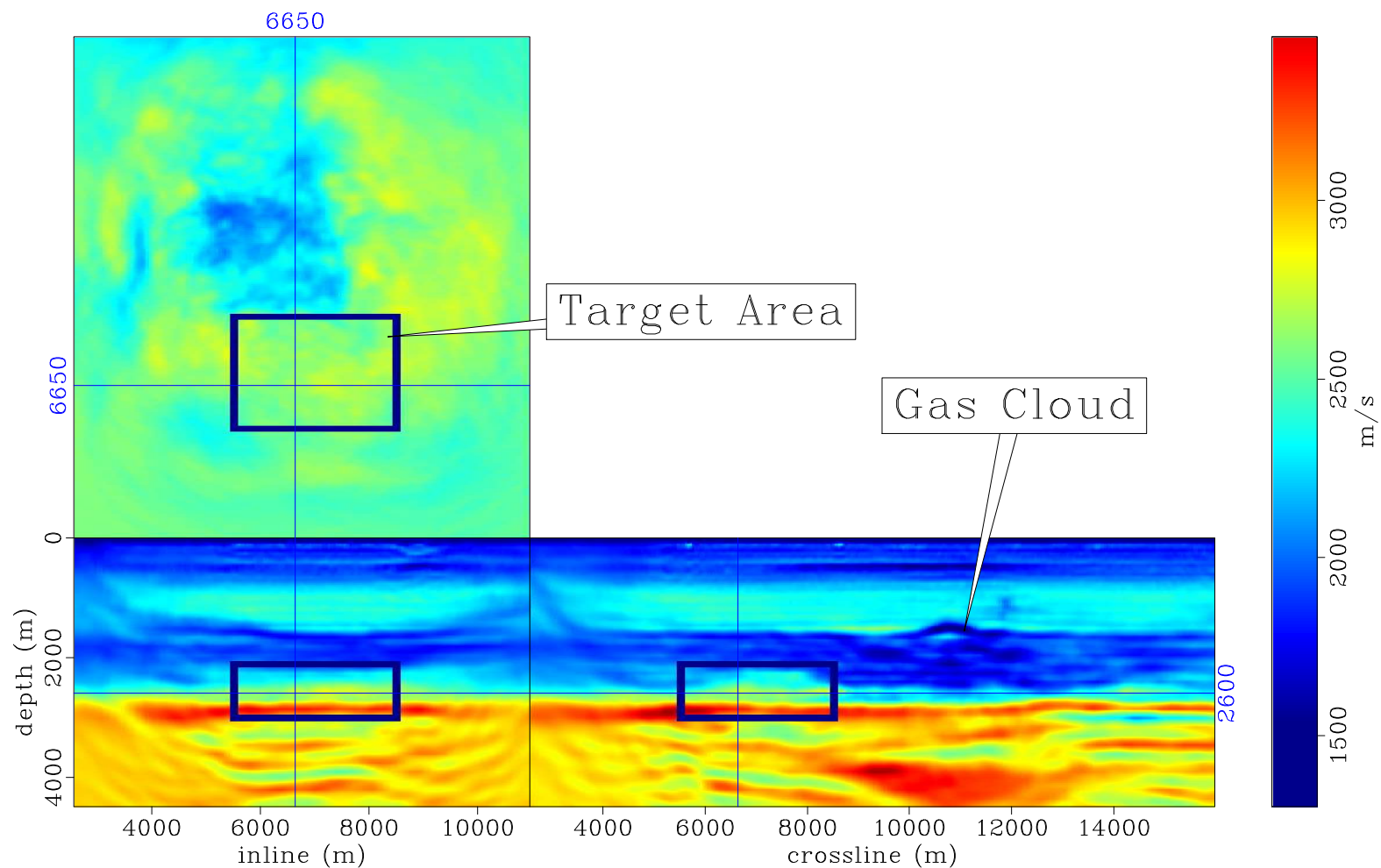


Figure 6.1: Baseline migration velocity obtained by full waveform inversion (see Sirgue et al. (2010)). This velocity model was used to image all data sets in this study. The target area—indicated by the box—is restricted to a small area of interest around the reservoir. The gas cloud, located outside the study area, does not cause significant imaging challenges in the target area. [NR] chap6/. vel-11

Figure 6.2 shows the full acquisition geometry of the Valhall LoFS project and the location of the study area considered in this chapter. Whereas the original (full) data consists of approximately 50,000 shots and 2,400 receivers, the available data subset consists of approximately 33,000 shots and 470 receivers. Figure 6.3 shows the geometry for the data subset, and the location of a gap within the study area that represents a simulated obstruction in the monitor geometry (described in detail later in Figure 6.6).

An enlarged view of the source-receiver geometry within the study area (Figure 6.3) is presented in Figure 6.4. The shots are spaced at 50 m in both the inline and crossline directions, while the receivers, located along 10 permanent cables, are spaced at 50 m in the inline and 300 m in the crossline directions (Figure 6.4). The receiver cables are buried at a depth from the water surface of approximately 70 m. For the data subset used in this chapter, the maximum absolute source-receiver offset is approximately 5 km.

The donor (BP) has adequately preprocessed these data sets, such that only the up-going primary compressional wave data are preserved. Therefore, unlike in the previous chapter, no additional preprocessing is applied to these data prior to migration. Examples of the preprocessed receiver gathers from the first survey (LoFS 1) and the ninth survey (LoFS 9) are presented in Figure 6.5. As shown in Figure 6.5, these receiver gathers, which are from the same location in the two surveys, contain data from the full range of azimuths.

The setup of the LoFS acquisition geometry allows for good repeatability of both source and receiver positions between surveys. For each survey, the source positions are repeated almost perfectly, with a standard deviation of approximately 5 m. Because the receiver cables are permanently installed, the receiver locations are repeated to a high degree of accuracy for all surveys. For this study, results from the original geometry provide a good reference to which results obtained from simulated problems in the recording geometry can be compared. Furthermore, the good source-receiver geometry repeatability allows testing of geophysical effects that are not associated with the data recording.

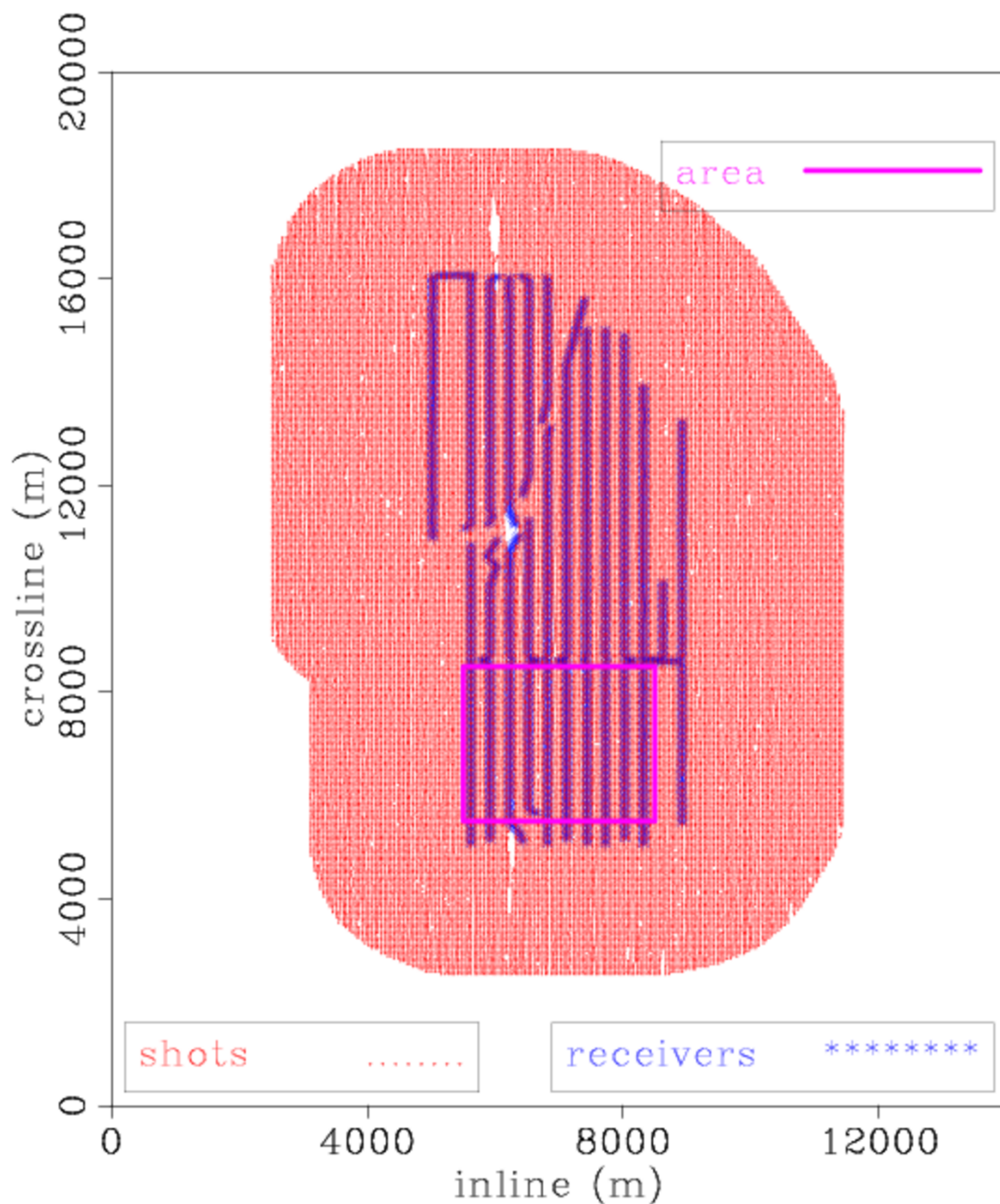


Figure 6.2: Full LoFS acquisition geometry showing locations of all shots and receivers. The purple box indicates the location of the study area, shown in detail in Figure 6.3. The coordinate axes in these figures (and in all figures) are distances in meters. [ER] chap6/. sgorig-1

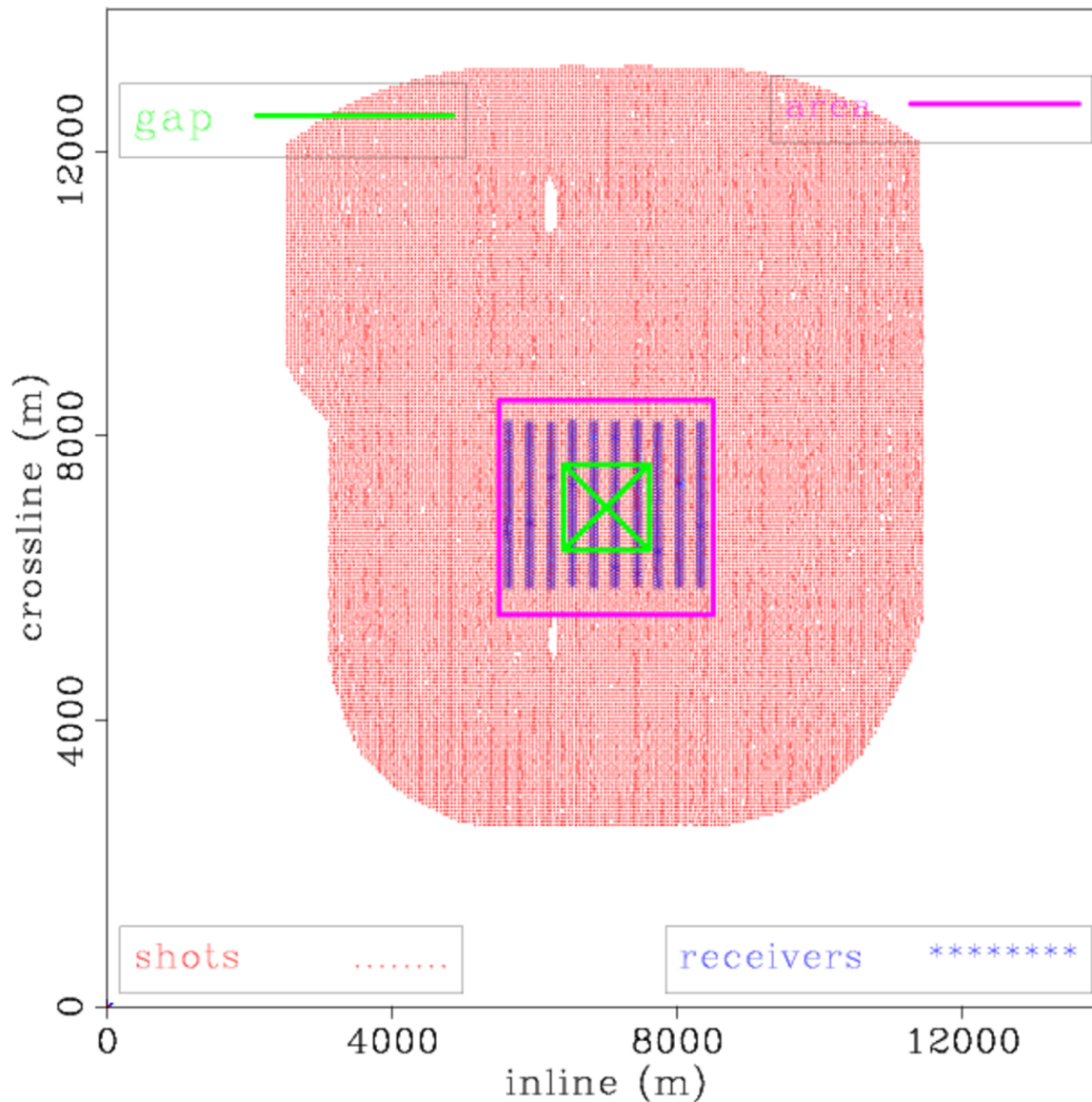


Figure 6.3: Acquisition geometry showing locations of all shots and receivers for the data subsets used in this study. Apart from the introduction of gaps in some examples, the source-receiver geometry is closely repeated for all data sets. The gap is located at the center of the study area (see Figure 6.6). An enlarged view of the study area is presented in Figure 6.4. [ER] `chap6/. sgfull-1-gap`

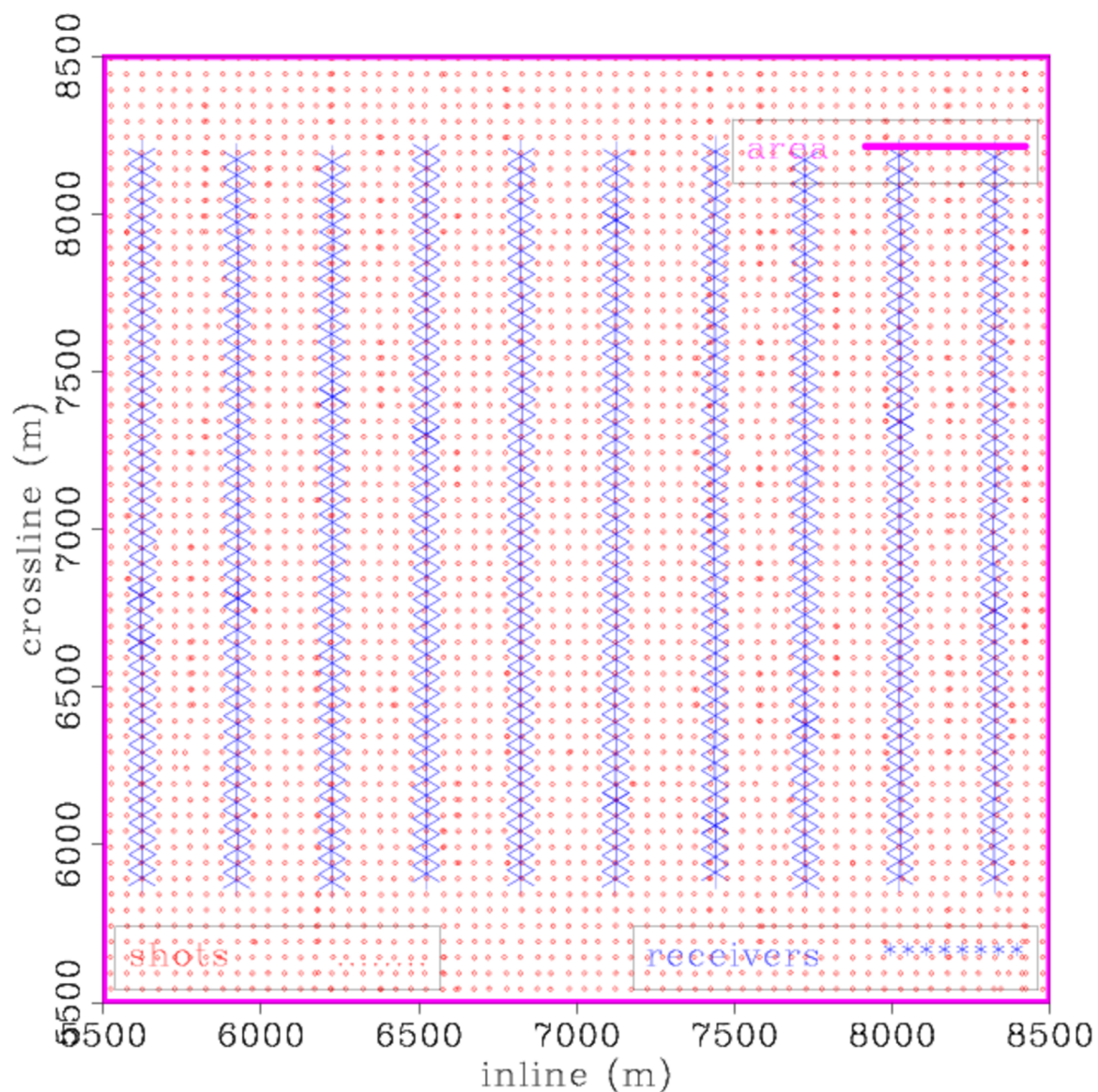


Figure 6.4: An enlarged view of the study area (Figure 6.3) showing the complete source-receiver geometry. The shot spacing is 50 m in both the inline and crossline directions, while the receiver spacing is 50 m in the inline direction and 300 m in the crossline direction. [ER] chap6/. sgwfull-1

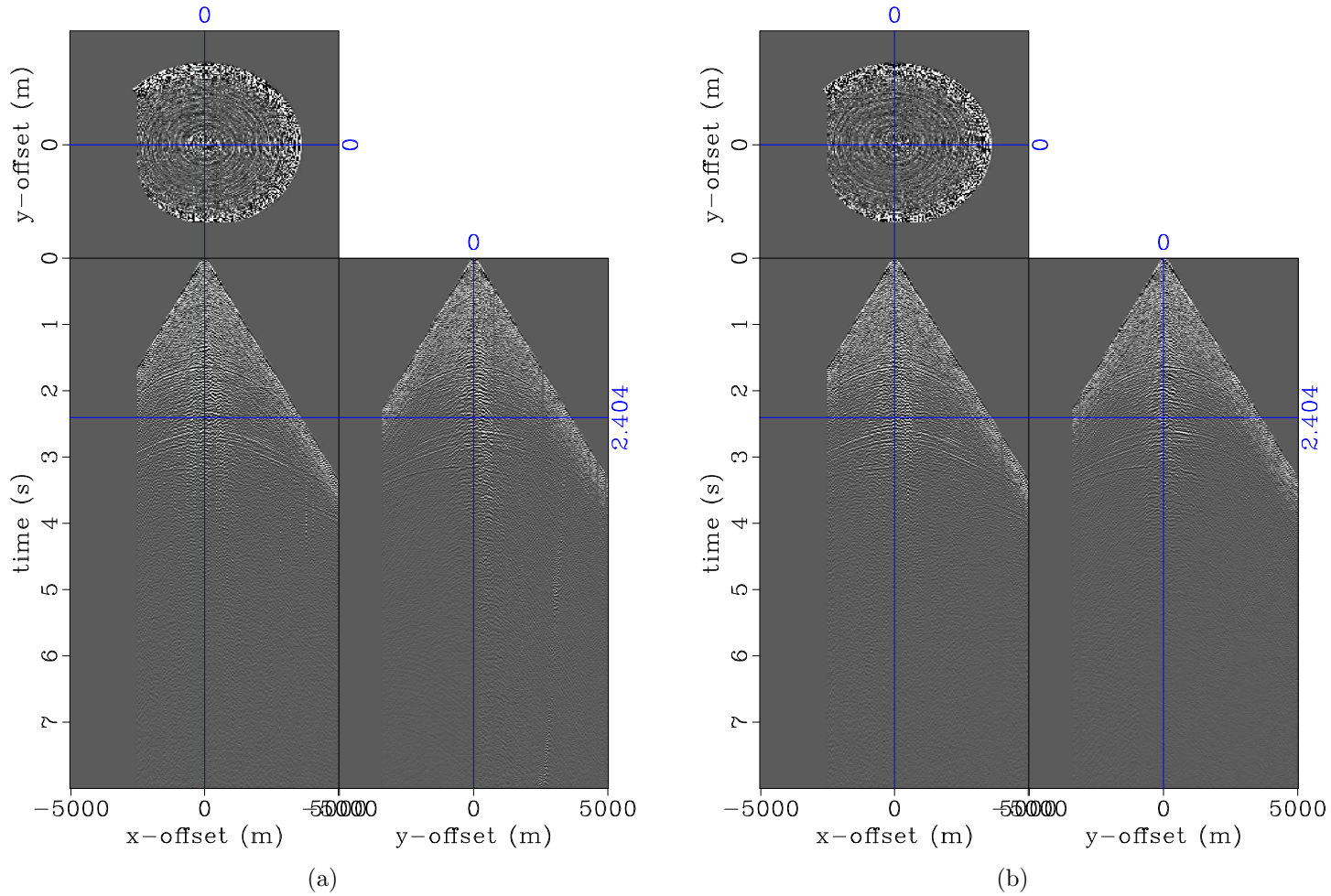


Figure 6.5: Sample receiver gathers acquired at the same location for the first (a), and ninth (b) LoFS surveys. Note in both gathers the full azimuth of the recording geometry. In both panels, the second and third dimensions are the inline and crossline offsets, respectively. [ER] chap6/. shot-11,shot-19

In the following sections, I present three examples that demonstrate applications of regularized joint image-domain inversion:

- First, using two data sets from the first and ninth LoFS surveys, as in the previous chapter, I show how regularized joint image-domain inversion can be used to attenuate artifacts that are caused by a simulated obstruction in the monitor geometry. This example shows that inversion of these incomplete data provides time-lapse amplitudes that are comparable to those obtained from the complete data.
- Second, using three data sets from the first, fifth, and ninth surveys, I show how regularized joint image-domain inversion can be applied to multiple data sets. In this example, as in the previous, I assume that these three surveys have different geometries caused by the presence of simulated obstructions in the monitor surveys. Recall that in chapter 4, I demonstrated an application of joint image-domain inversion to synthetic migrated images obtained by multiplying the Hessian matrices corresponding to these three surveys with synthetic reflectivity images.
- Third, using the complete data from the first and ninth surveys, I demonstrate that because of its high computational efficiency, regularized joint image-domain inversion method can be used to obtain multiple realistic time-lapse images by choosing multiple regularization parameters. This is advantageous because it allows the testing of different geological and petrophysical scenarios that might explain the changes observed in the acoustic properties of the reservoir and surrounding rocks. This can help in the quantification of uncertainties associated with interpretation of the time-lapse seismic data.

These examples demonstrate that regularized joint image-domain inversion is an effective tool for obtaining time-lapse seismic images that have better resolution, better quality, and higher reliability than those obtained from conventional imaging by migration.

Example I: Inversion of incomplete data

In this section, I consider data from the first survey (LoFS 1) and the ninth survey (LoFS 9), acquired in November 2003 and December 2007, respectively. In this example (and in other examples presented in this chapter), LoFS 1 is the baseline.

To simulate an obstruction in the monitor geometry, I create a 1.44 km² gap at the center of the 9 km² study area (Figures 6.3). Figure 6.6 shows an enlarged view of the study area indicating the location of the simulated obstruction. As shown in Figure 6.6, in order to maximize the geometry difference between the baseline and monitor surveys, no shots and receivers are present within the obstruction area in the monitor geometry.

Figure 6.7 shows the common-midpoint (CMP) fold for the complete (baseline) and incomplete (monitor) geometries. The highest fold is approximately 1,900 in the baseline geometry (Figure 6.7(a)), whereas it is approximately 1,600 in the monitor geometry (Figure 6.7(b)). Because of the full azimuth coverage of the recording geometry, these CMP folds are higher than those in typical seismic surveys. As shown in Figure 6.7, the differences in fold between the two geometries are largest within the obstruction area. Although CMP folds provide a measure of the geometry difference, as I will show later, differences in subsurface illumination associated with such geometry difference are too complex to be represented by CMP fold differences.

Subsurface illumination (Hessian diagonal) of study area

As described in previous chapters, one measure of the subsurface illumination is the diagonal of the Hessian. For both geometries, I compute the diagonal of the Hessian for the study area using 64 frequencies, which are spaced equally within the migration frequency band (described later in this section). In this and in other examples presented in the chapter, I use the random phase-encoded approximation of the Hessian defined in equation 3.12 and described in detail by Tang (2011). For each geometry, I use four random realizations of the receiver-side Green's functions.

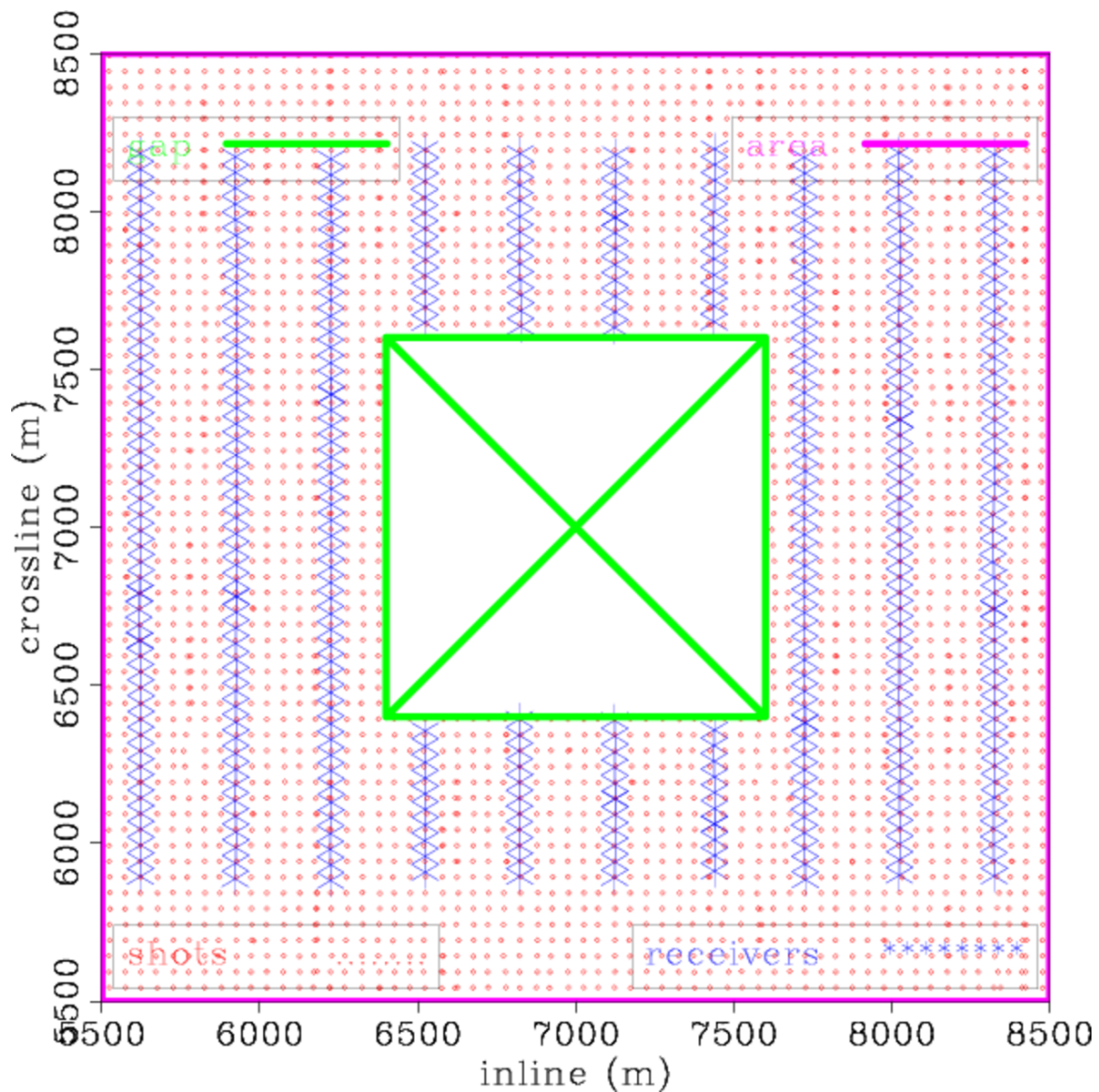


Figure 6.6: An enlarged view of the study area (Figure 6.3) showing the shot and receiver locations within the study area, and the location of the simulated obstruction in the monitor geometry. There are not sources and receivers within the gap. Compare this to Figure 6.4, which shows the complete geometry of the baseline survey. [ER]

chap6/. Osgwfull-9-gap

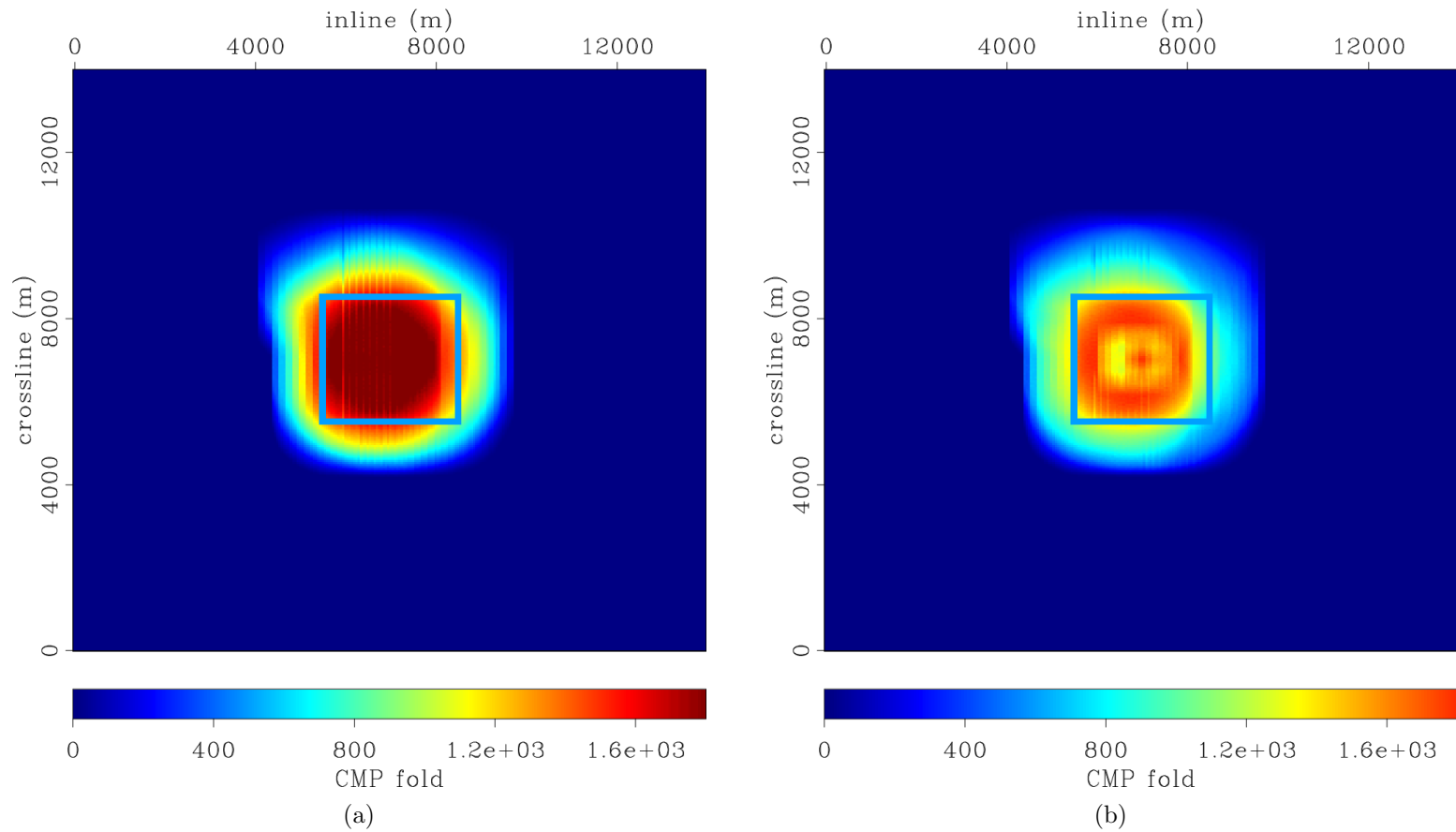


Figure 6.7: Surface (CMP) fold for the baseline (a) and monitor (b). Red indicates high fold, whereas blue indicates low fold. Note that whereas the baseline fold is mostly uniform within the study area, the gapped monitor geometry causes significant non-uniformity of fold. The box indicates the same study area shown in Figures 6.3. [ER]

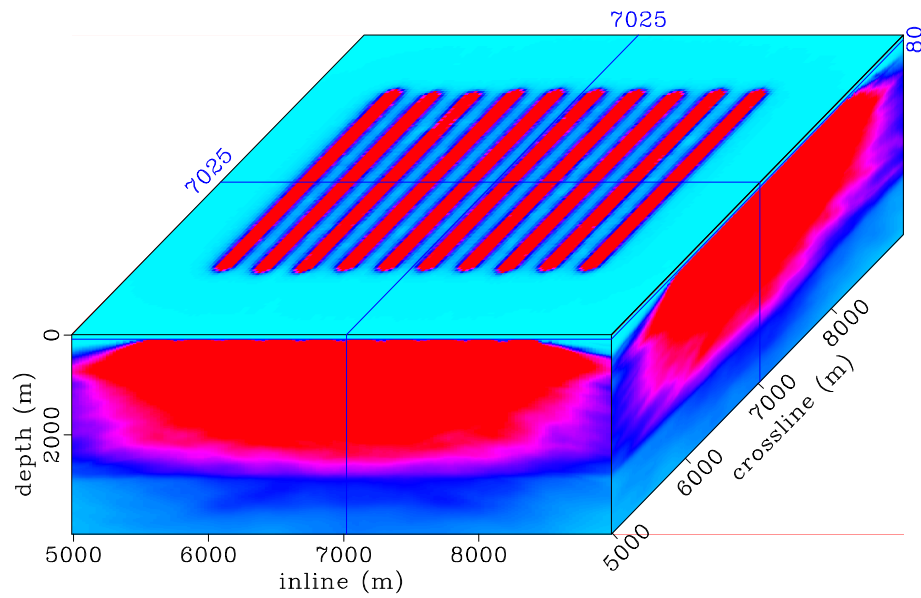
chap6/. cfold-1-full,cfold-9-gap

The subsurface illumination of the study area for the baseline and monitor geometries are presented in Figures 6.8 to 6.10. Figure 6.8 shows the subsurface illumination with a depth slice at the ocean bottom. The locations of the 10 receiver cables, and of the simulated obstruction can be seen clearly in Figure 6.8. Figure 6.9 shows the subsurface illumination with a depth slice at 1,750 m, above the reservoir and outside the target area for inversion. The subsurface illumination for the two geometries showing a depth slice through the reservoir at 2,600 m, is presented in Figure 6.10. In general, the subsurface illumination increases in complexity with depth. In both the baseline and monitor geometries, the subsurface illumination distribution is highly non-stationary throughout the study area.

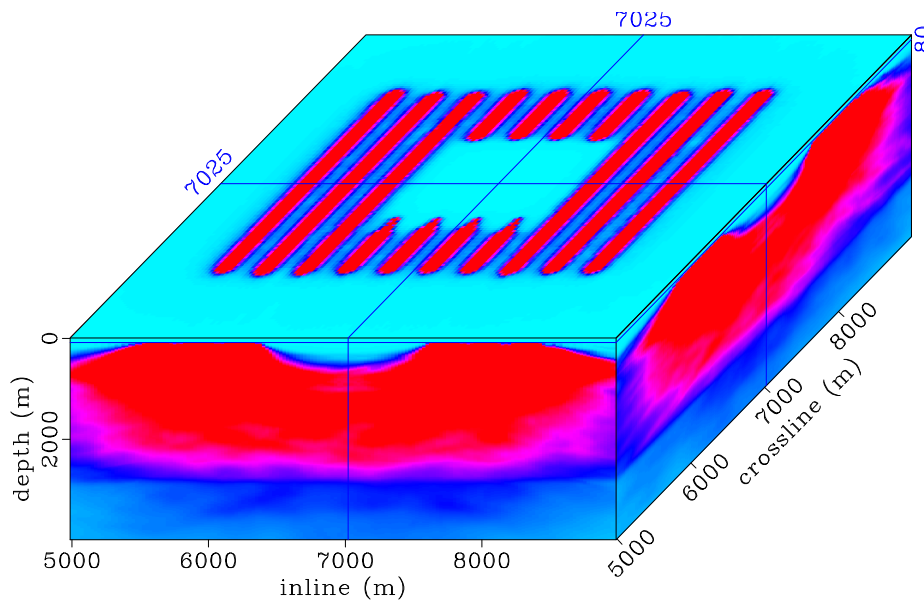
To measure the difference in subsurface illumination, I compute the ratio of the subsurface illumination between the baseline and monitor geometries. The illumination ratio is presented in Figure 6.11 with depth slices at the ocean bottom and at the reservoir depth. Although the illumination discrepancy is simple at the ocean bottom (Figure 6.11(a)), it becomes highly complex at the reservoir depth (Figure 6.11(b)). Comparing this subsurface illumination ratio with the difference in surface CMP folds (Figure 6.7), it is clear that it is impossible to fully account for the geometry difference using information derived from only CMP folds. However, as shown in chapter 4, one important limitation in the use of the Hessian diagonal as a weighting function to correct for illumination discrepancies in migrated images is that it applies equal weights to all illuminated wavenumbers/angles. To obtain more complete information about differences in the dip-dependent subsurface illumination between surveys, in the next section, I compute the off-diagonal elements of the Hessian matrices.

Hessian matrix of the target area

The target area for inversion is a small (700 x 3000 x 3000 m) window around the reservoir, located within the study area (Figure 6.1). For this target area, I compute the approximate Hessian using 64 frequencies and six random realizations of the receiver-side Green's functions. At each subsurface location within the target area, the off-diagonal elements (PSFs) are 300 x 300 x 300 m in size.

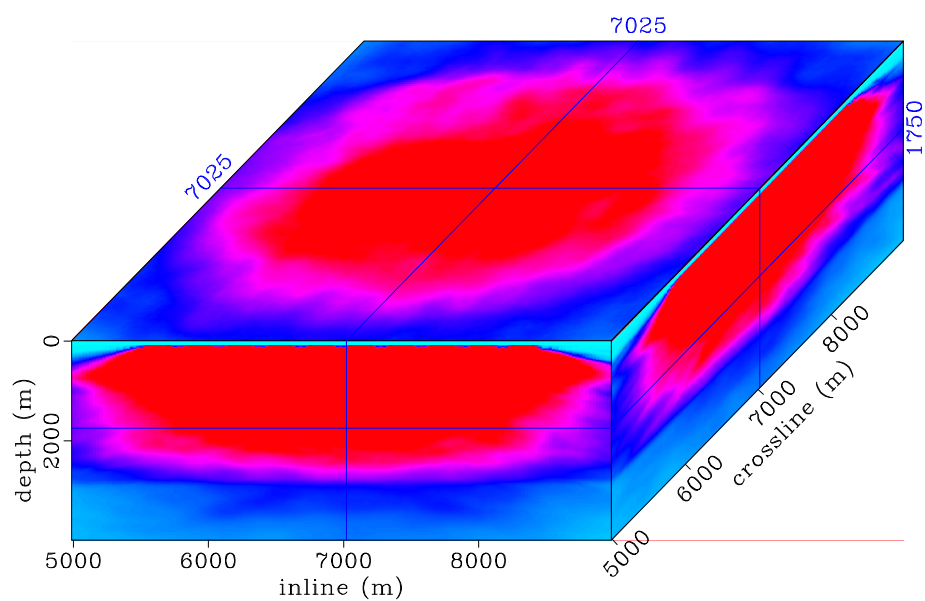


(a)

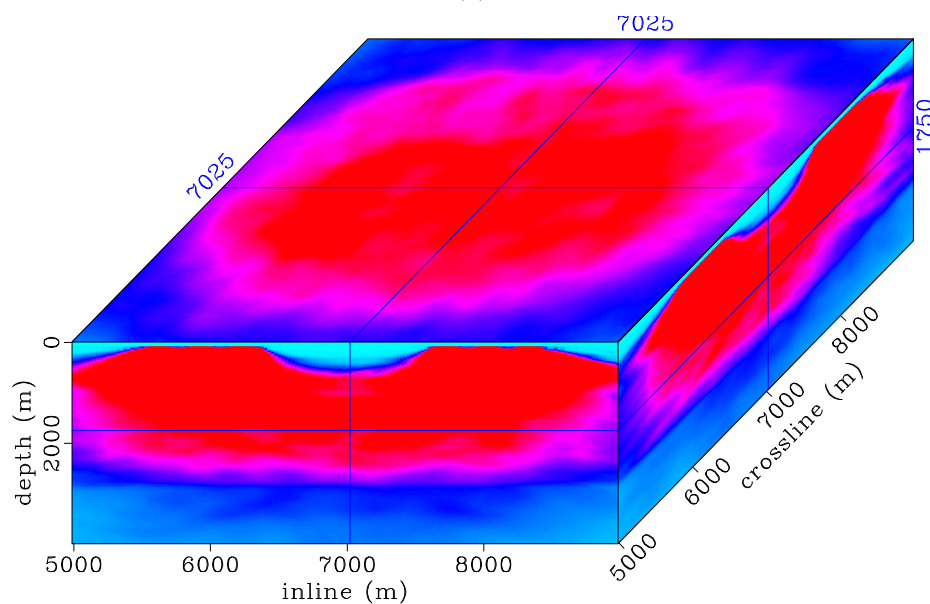


(b)

Figure 6.8: Hessian diagonal for the complete baseline (a) and incomplete monitor (b) geometries. In these (and similar) displays throughout this chapter, the top panel is a depth slice and the side panels are the inline and crossline slices. The crosshairs show the position of the slices in the image cube. The depth slices show the illumination at the ocean bottom (a) and (b). Red indicates high illumination, whereas cyan indicates low illumination. [CR] chap6/. ilum-1,ilumg2-1

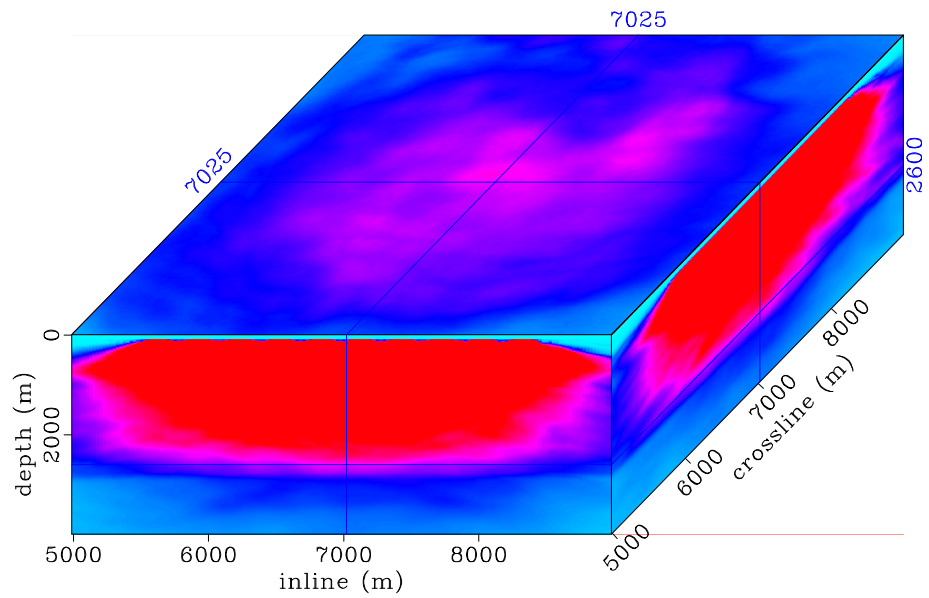


(a)

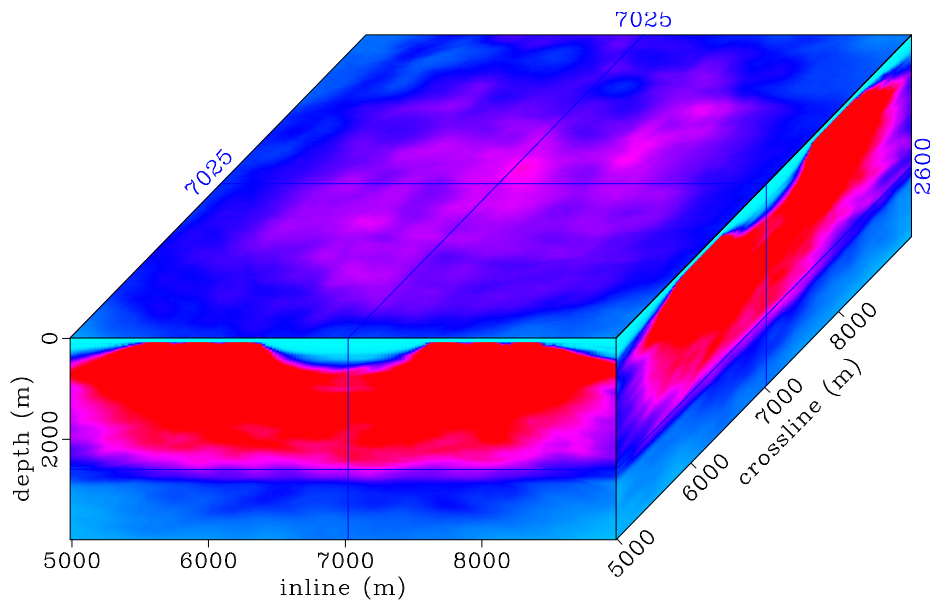


(b)

Figure 6.9: Hessian diagonal for the complete baseline (a) and incomplete monitor (b). The depth slices show the illumination at a depth the above the reservoir. Red indicates high illumination, whereas cyan indicates low illumination. [CR] chap6/. ilum-3,ilung2-3

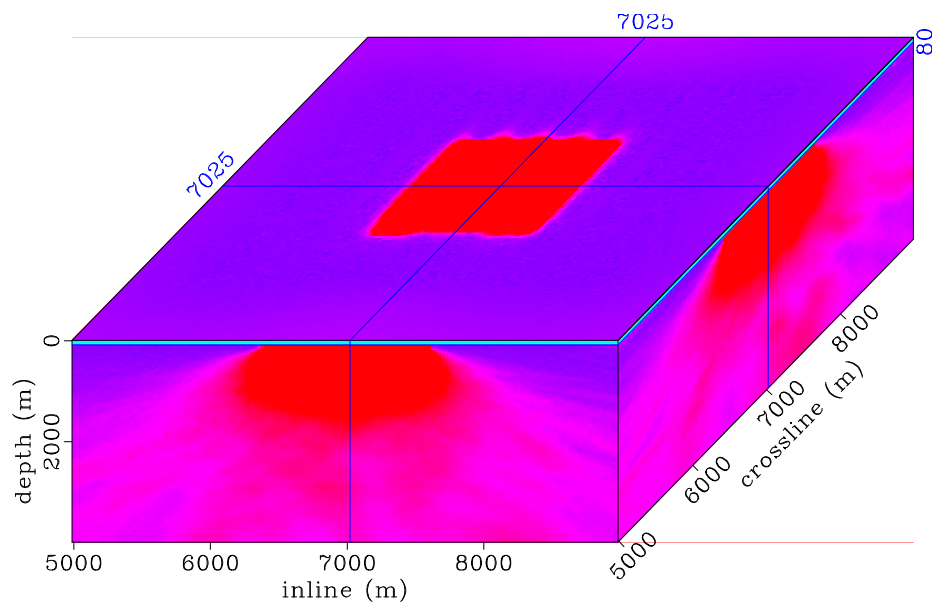


(a)

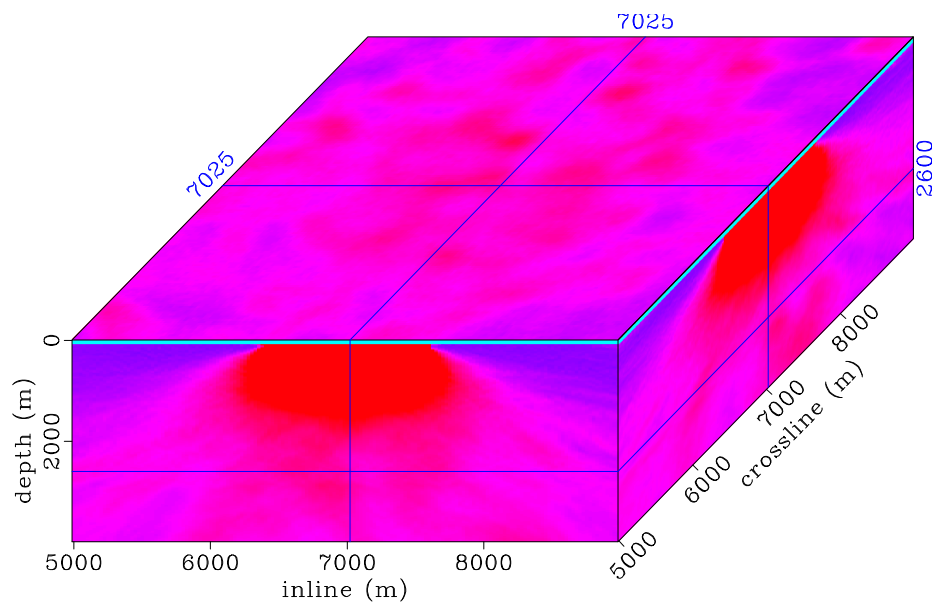


(b)

Figure 6.10: Hessian diagonal for the complete baseline (a) and incomplete monitor (b). The depth slices show the illumination within the reservoir. Red indicates high illumination, whereas cyan indicates low illumination. [CR] chap6/. ilum-4,ilumg2-4



(a)



(b)

Figure 6.11: Illumination ratio between the baseline and monitor at the ocean bottom (a) and at the reservoir depth (b). Note that the simple rectangular illumination disparity at the ocean bottom becomes more complex at the reservoir depth. [CR] chap6/. ilumr2-1,ilumr2-4

Figure 6.12 shows an example of the off-diagonal elements along the a row the Hessian matrix (PSF) derived from the baseline geometry in the spatial and wavenumber domains. As shown in Figure 6.12(b), at this subsurface position, the baseline ge-

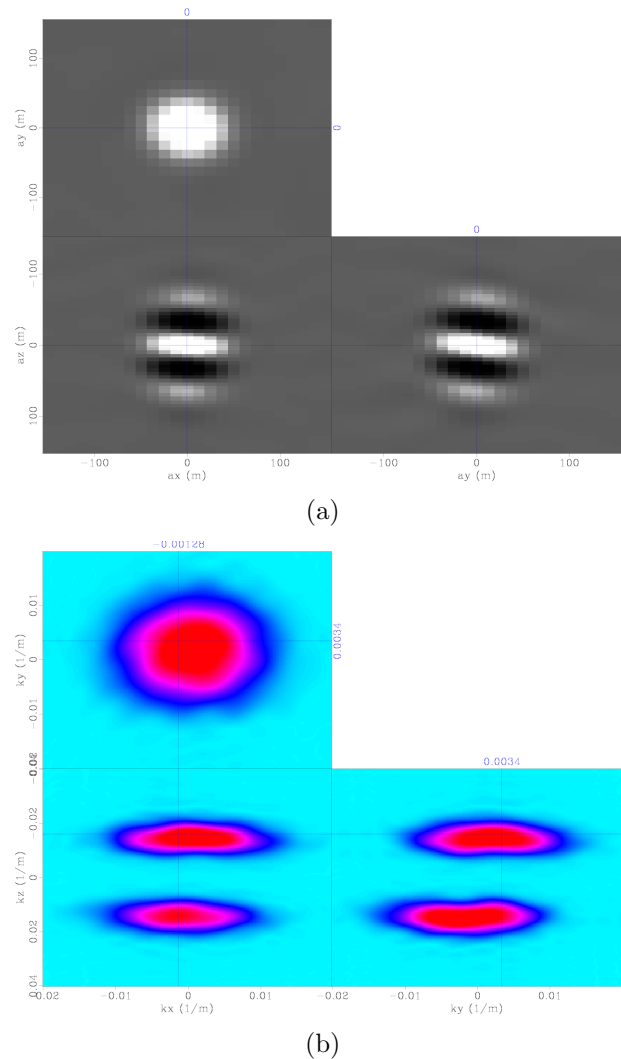


Figure 6.12: Point spread function (row of the baseline Hessian matrix) at subsurface point inline 6,600 m, crossline 6,475 m and depth 2,580 m in the spatial domain (a), and in the wavenumber domain (b) for the complete (baseline) geometry. [CR] chap6/. 3d3-psf-1,3d3-psf-fft-1

ometry provides sufficient coverage in all directions. Figure 6.13 shows the difference between the baseline and monitor PSFs in the spatial and wavenumber domains. As

shown in Figure 6.13(b), the gap in the monitor geometry (Figure 6.6) leads to incomplete illumination of various wavenumbers. Instead of equal weighting assumed by

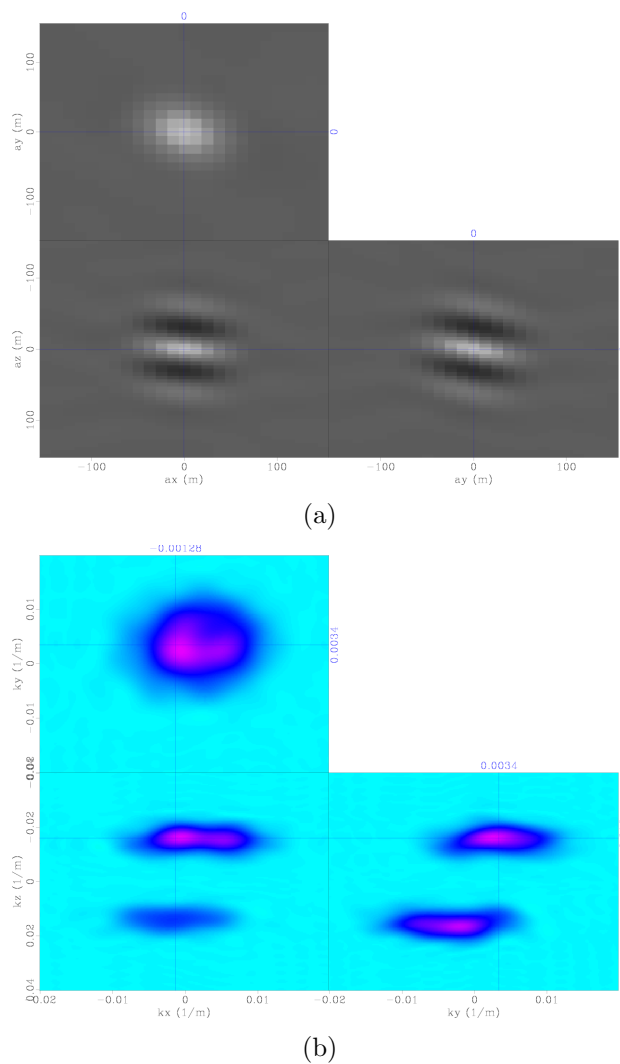


Figure 6.13: Difference between the baseline point spread function at subsurface point inline 6,600 m, crossline 6,475 m and depth 2,580 m (Figure 6.12) and the monitor point spread function at the same point in the spatial domain (a), and in the wavenumber domain (b). [CR] `chap6/. 3d3-psf-19,3d3-psf-fft-19`

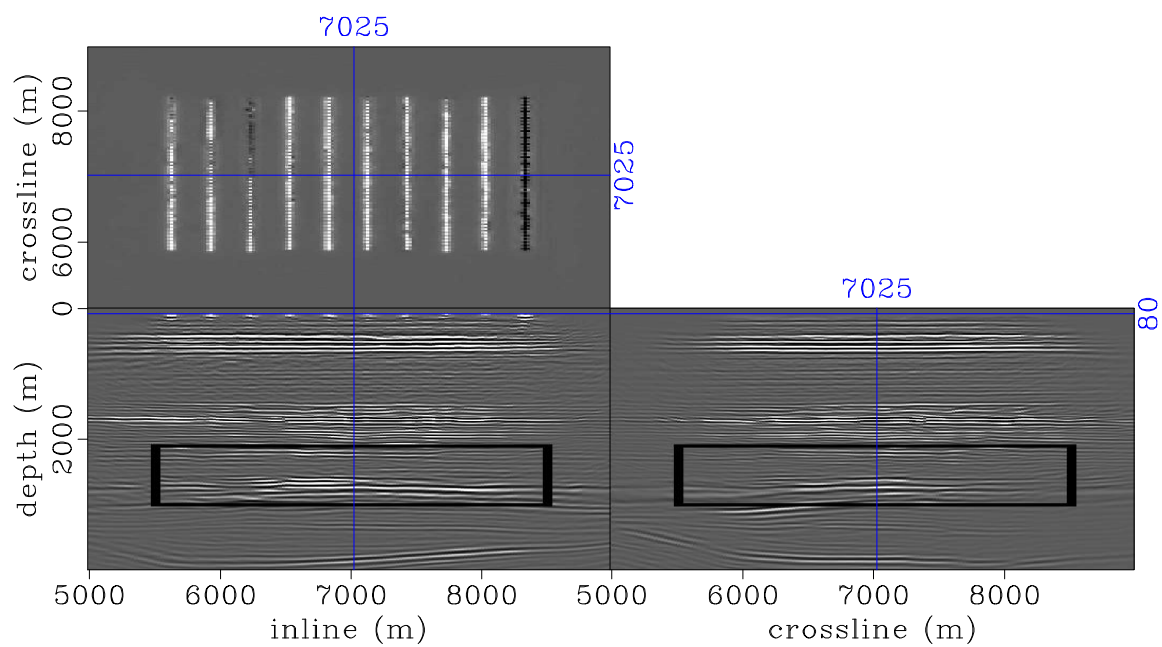
the use of only the diagonal of the Hessian, the off-diagonal elements allow accurate compensation of illumination discrepancies for different wavenumbers.

Migration

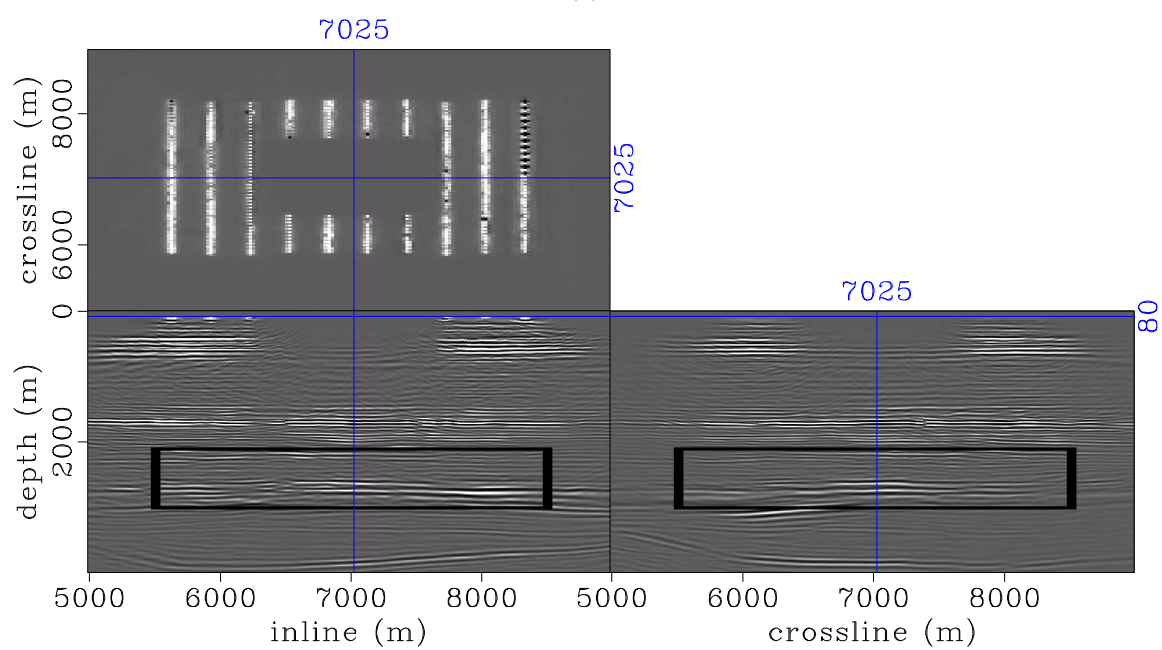
Using reciprocity, the shot and receiver locations are swapped, such that for imaging purposes, the receiver gathers are treated as shot records. Recall that examples of these full-azimuth receiver gathers were presented in the previous section (Figure 6.5). The data are migrated using 320 equally spaced frequencies up to 35 Hz with a split-step one-way wave-equation shot-profile migration algorithm. The same propagator was used to compute the Hessian described above. Both the baseline and monitor data sets are migrated with the baseline velocity model (Figure 6.1). This velocity model was obtained to a high degree of accuracy—a requirement for the regularized inversion method—thereby providing high-quality imaging of the study area. The migrated baseline and monitor images, showing different depth slices through key formations, are presented in Figures 6.14 to 6.17.

Figure 6.14 shows the migrated baseline and monitor images with depth slices at the ocean bottom. As in the images of the subsurface illumination (Figure 6.8), the positions of the receiver cables and the location of the rectangular gap in the monitor geometry—created by a simulated obstruction—can be seen clearly. Figure 6.15 shows the migrated baseline and monitor images with depth slices at 500 m, showing the locations of shallow faults in the area. Comparing Figure 6.15(b) to Figure 6.14(b), note that at this depth, the effect of the gap on the migrated monitor image has reduced. Figure 6.16 shows the migrated baseline and monitor images with depth slices at 1,750 m, showing clear images of a dominant faulted and channelized unconformity above the reservoir. At this depth, differences between the baseline and monitor images have been further reduced.

The migrated images showing a depth slice through the reservoir are presented in Figure 6.17. At the reservoir depth, differences between the baseline and monitor images are a combination of the effects of geometry difference, and of production- and injection-induced changes in reflectivity. In this example, the goal is to account for geometry difference between the surveys, while preserving production- and injection-induced changes in reflectivity between the baseline and monitor images.

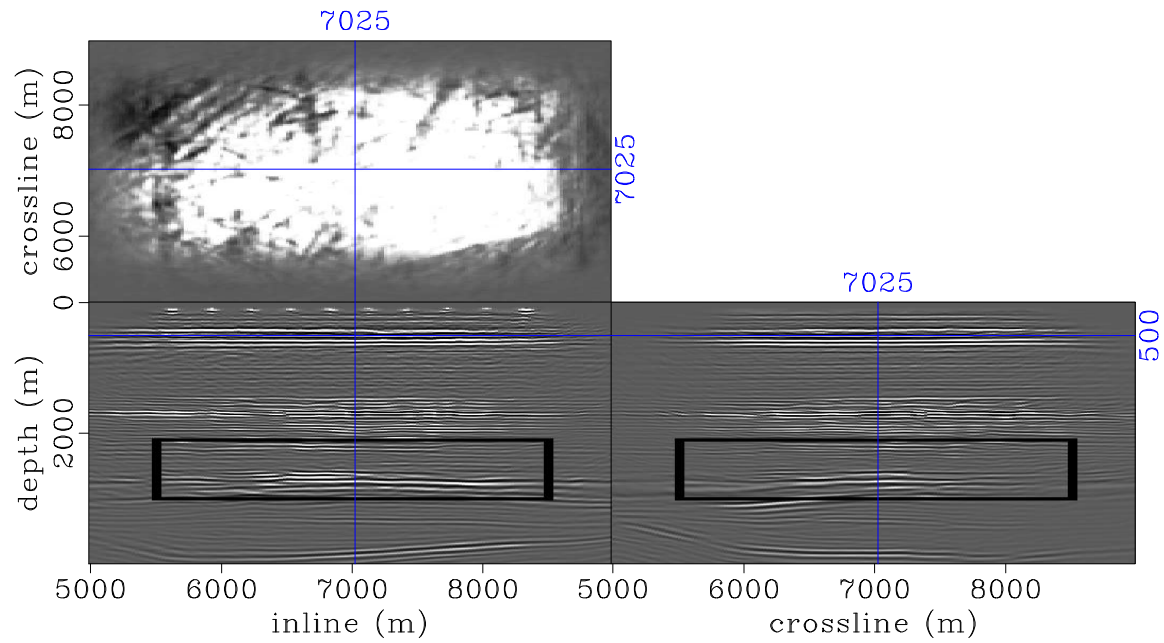


(a)

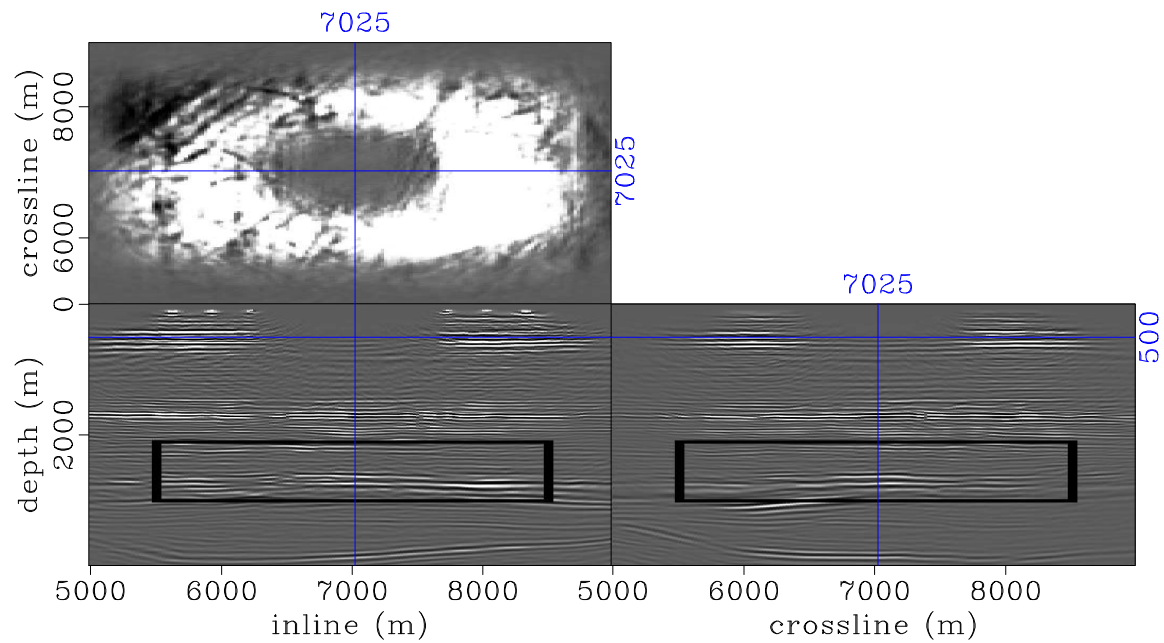


(b)

Figure 6.14: Migrated images showing depth slices at the ocean bottom. The box indicates the target area in the baseline image (a) and in the monitor image (b). Note the location of the gap in the monitor. [CR] chap6/. mig-1-box,migg-1-box

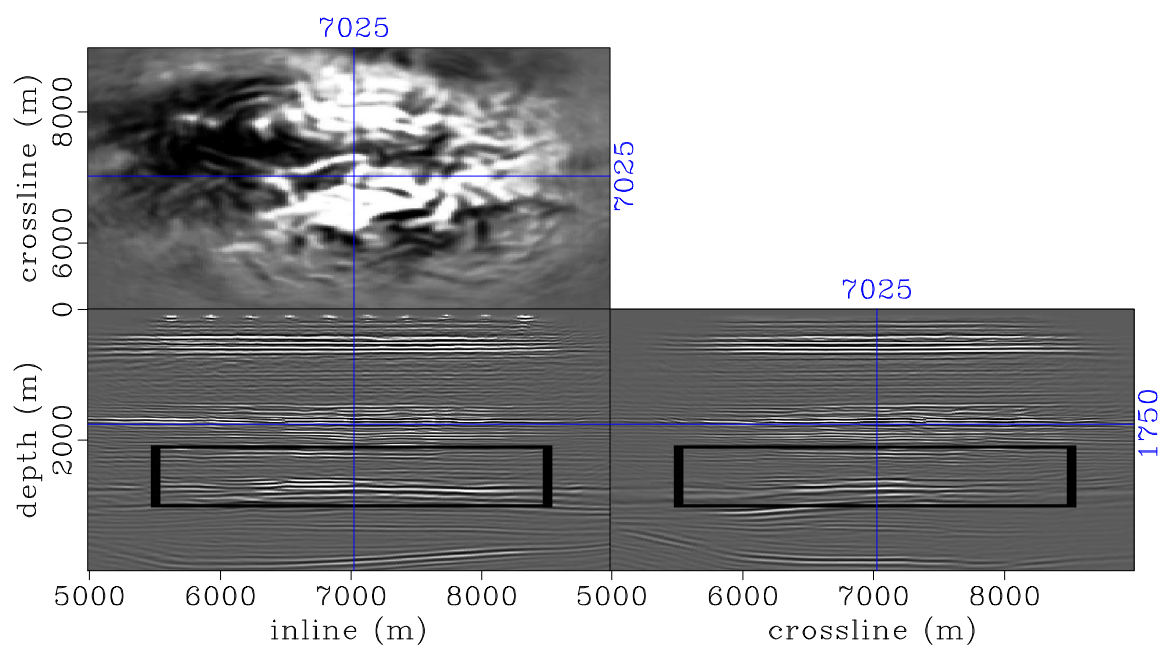


(a)

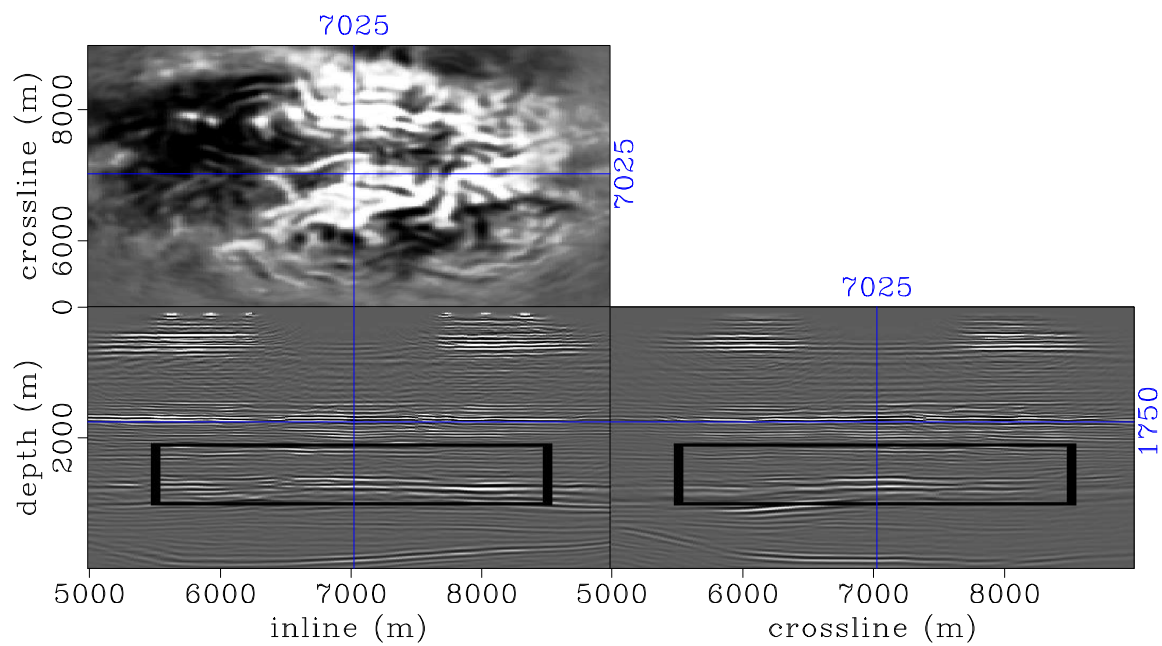


(b)

Figure 6.15: Migrated images showing depth slices at 50 m. The box indicates the target area in the baseline image (a) and in the monitor image (b). The shallow faults at this depth are clearly imaged. [CR] chap6/. mig-2-box,migg-2-box



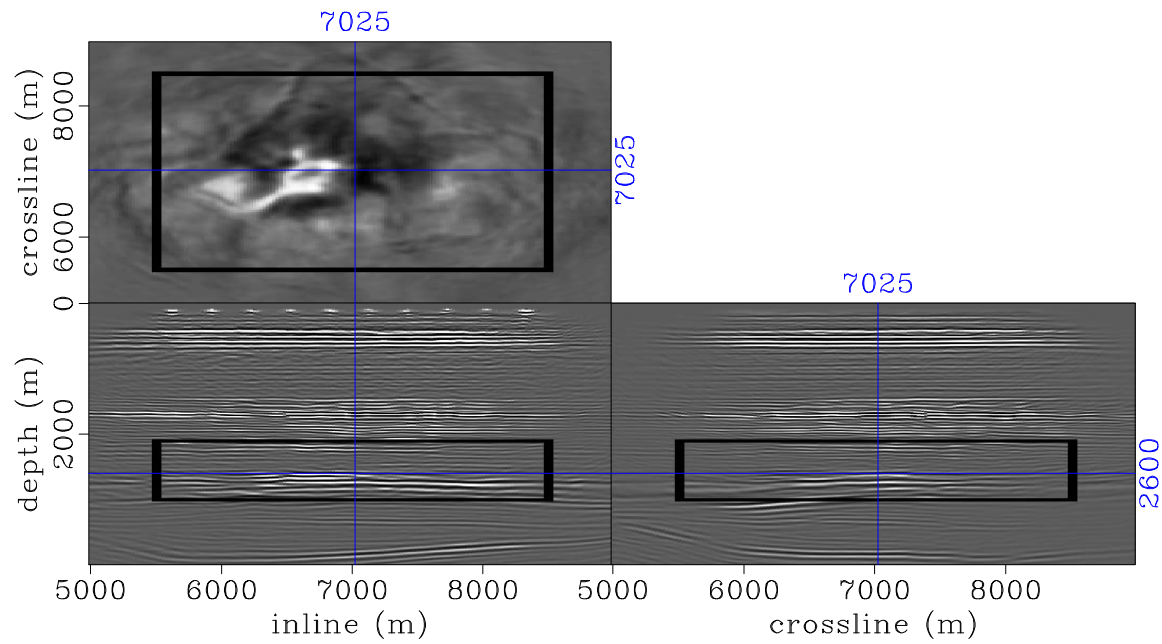
(a)



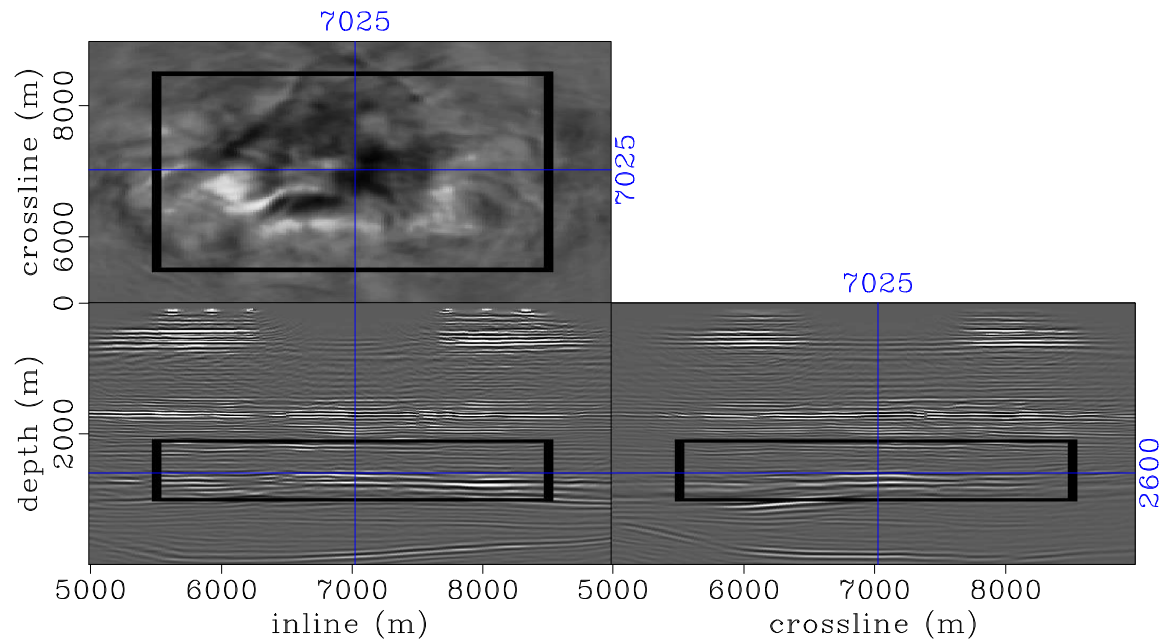
(b)

Figure 6.16: Migrated images showing depth slices above the reservoir at 1,750 m. The box indicates the target area in the baseline image (a) and in the monitor image (b). The well-imaged unconformity show evidence of faulting and channelization.

[CR] chap6/. mig-3-box,migg-3-box



(a)



(b)

Figure 6.17: Migrated images showing depth slices at the reservoir depth. The box indicates the target area in the baseline image (a) and in the monitor image (b). In (a) and (b), the flanks of the Valhall structure are imaged clearly. [CR]

chap6/. mig-4-box,migg-4-box

The boxes in the migrated images (Figures 6.14 to 6.17) indicate the location of the target area. This target area, was chosen to include the reservoir and surrounding rocks. Figure 6.18 shows the migrated baseline and monitor images of the target area, obtained from complete and incomplete geometries respectively. The time-lapse image obtained as the difference between these images is presented in Figure 6.19.

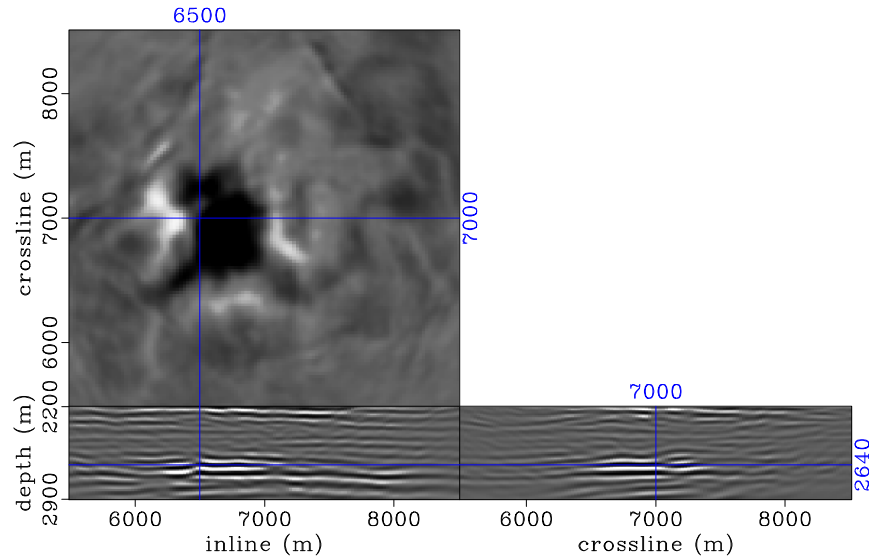
Multidimensional warping

As discussed earlier, we expect that hydrocarbon production and water injection in the reservoir will cause fluid changes and pressure depletion. These will lead to velocity changes and compaction between surveys. Therefore, migrating the monitor data with the baseline velocity causes apparent displacements between the baseline and monitor images. As a result, the time-lapse image in Figure 6.19 contains amplitude differences that are caused not only by production and geometry effects, but also by misalignments between the images associated with velocity changes and compaction between surveys.

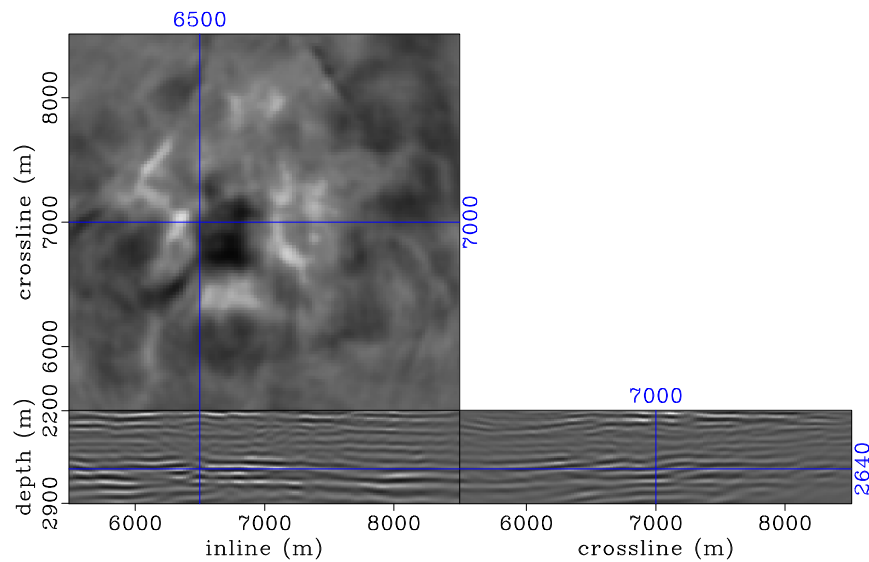
As in the previous chapter, before an interpretable difference image can be obtained between the baseline and monitor images, the apparent displacements must be removed. In addition, as described in chapter 3, removal of these apparent displacements from the migrated images ensures that all image points are collocated. Collocation of baseline and monitor image points is a prerequisite for the regularized joint image-domain inversion method developed in this dissertation.

I estimate the three-dimensional components of the apparent displacements between the baseline and monitor images using the sequential one-dimensional correlation method described in chapter 2. Figure 6.20 shows the vertical (depth) components of the apparent displacement vectors between the baseline image (Figure 6.18(a)) and the monitor image (Figure 6.18(b)). The corresponding inline and crossline components are presented in Figure 6.21.

Figure 6.22(a) shows the time-lapse image between the warped images. For comparison, Figure 6.22(b) shows the reference time-lapse image between the migrated



(a)



(b)

Figure 6.18: Migrated images of the target area obtained from the complete baseline data (a), and the incomplete monitor data (b). The time-lapse image between these images is shown in Figure 6.19. Compare these images to the inverted images in Figure 6.25. [CR] chap6/. gap-b4-mod1,gap-b4-mod2

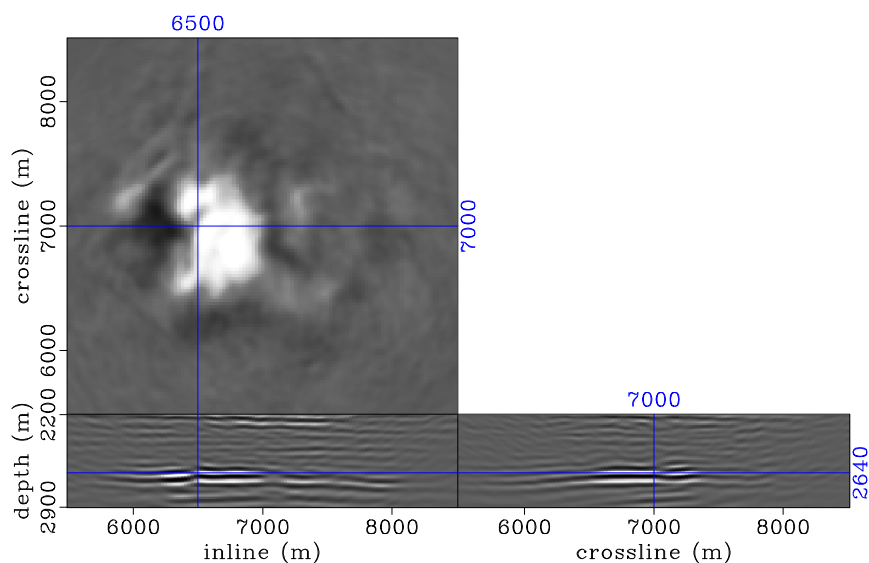


Figure 6.19: Time-lapse image obtained as the difference between the migrated baseline and monitor images (Figure 6.18) prior to warping. Compare this to the time-lapse image difference between the warped images (Figure 6.22(a)), and between the inverted images (Figure 6.24(a)). [CR] chap6/. gap-b4-d-mod

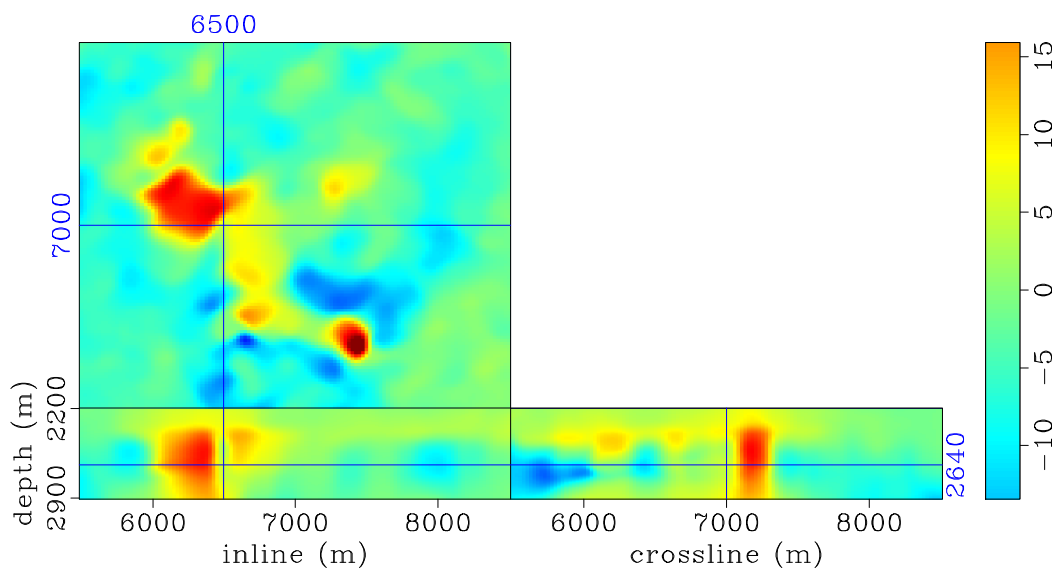
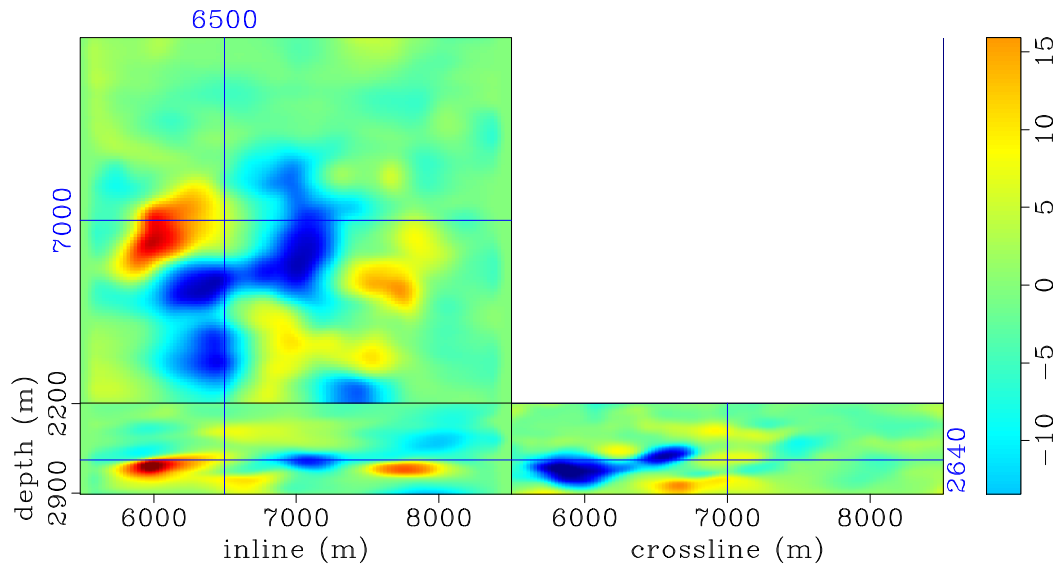
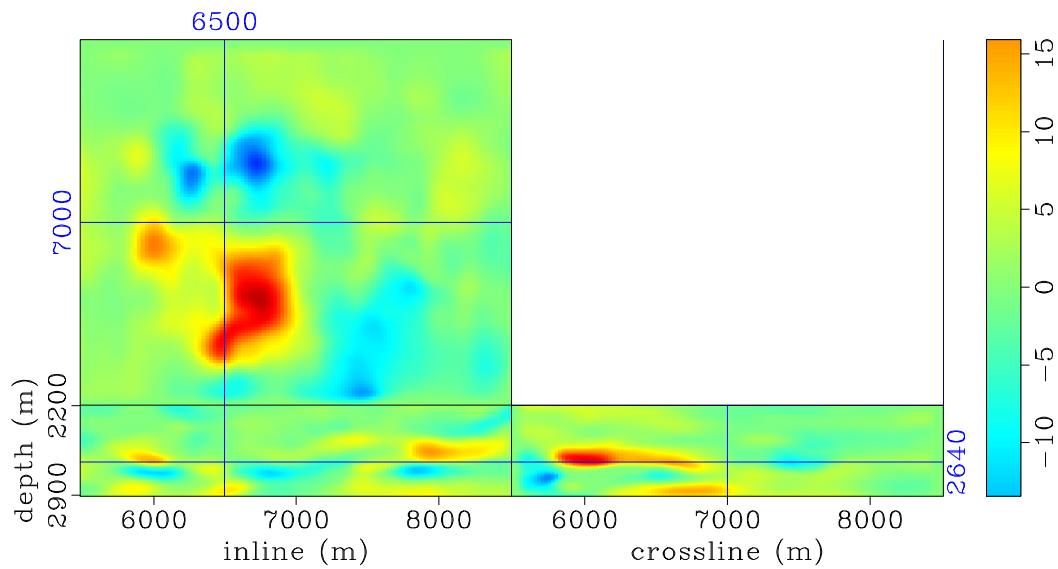


Figure 6.20: Vertical (a) components of apparent displacement vectors between the baseline and monitor images within the target area. Red indicates downward displacements, whereas blue indicates upward displacements. The inline and crossline components of these displacement vectors are presented in Figure 6.21. [CR] chap6/. ts-1



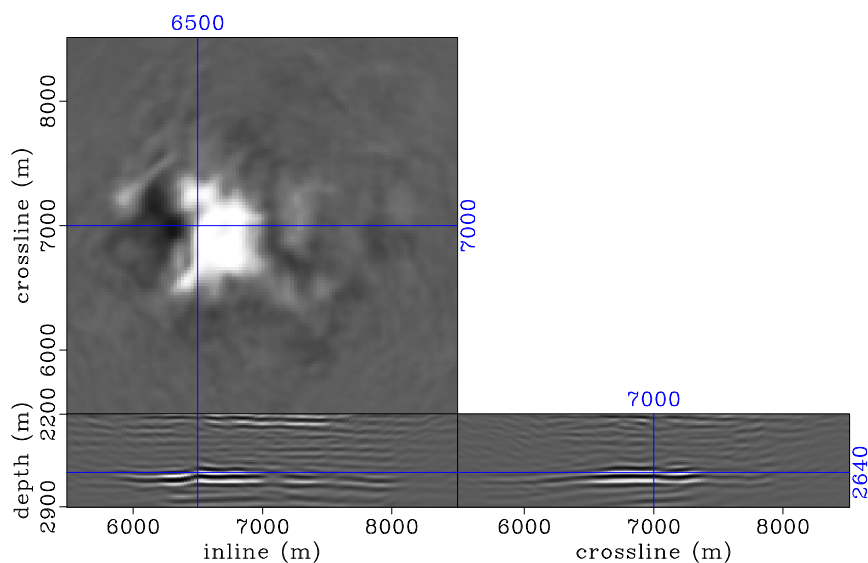
(a)



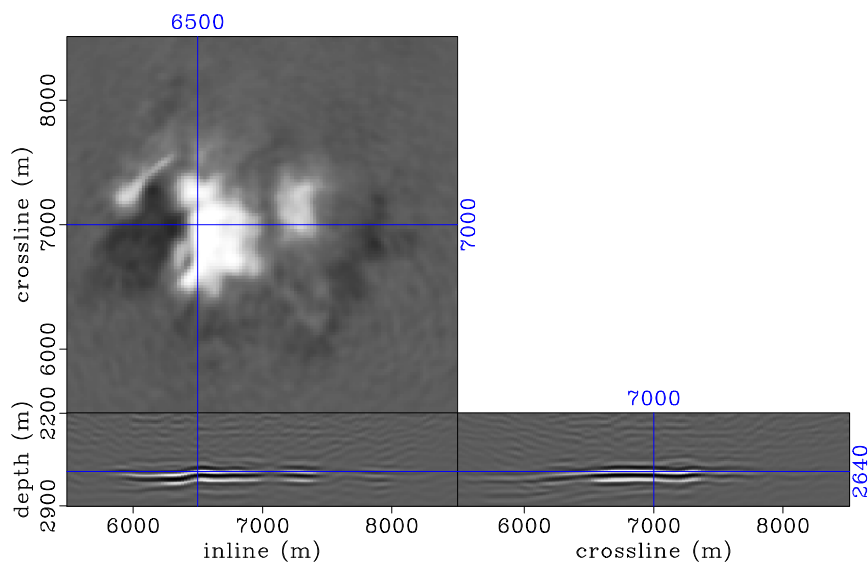
(b)

Figure 6.21: Inline (a) and crossline (b) components of apparent displacement vectors between the baseline and monitor images within the target area. In these figures, Red indicates rightward displacements, whereas blue indicates leftward displacements. The corresponding vertical (depth) components are shown in Figure 6.20. [CR]

chap6/. ts-2,ts-3



(a)



(b)

Figure 6.22: Migrated time-lapse images of the target area obtained after warping the monitor image to the baseline image. Panel (a) shows the time-lapse image derived from the complete baseline and incomplete monitor, whereas panel (b) shows the time-lapse image derived from complete baseline and complete monitor data sets. In (a), artifacts caused by misalignments due to velocity and compaction have been removed, leaving only differences due to production-induced reflectivity changes and difference in geometry between the baseline and monitor data. The differences between (a) and (b) are caused by the incomplete monitor geometry in (a). [CR]

chap6/. gap-d-mod,fine-d-mod

(and warped) baseline and monitor images derived from complete data sets. To obtain this reference time-lapse image, I migrate the complete baseline and monitor data using the same parameters applied to the incomplete data (described above). I then apply the same warping procedure as in Figure 6.22(a) to remove the apparent displacements between them.

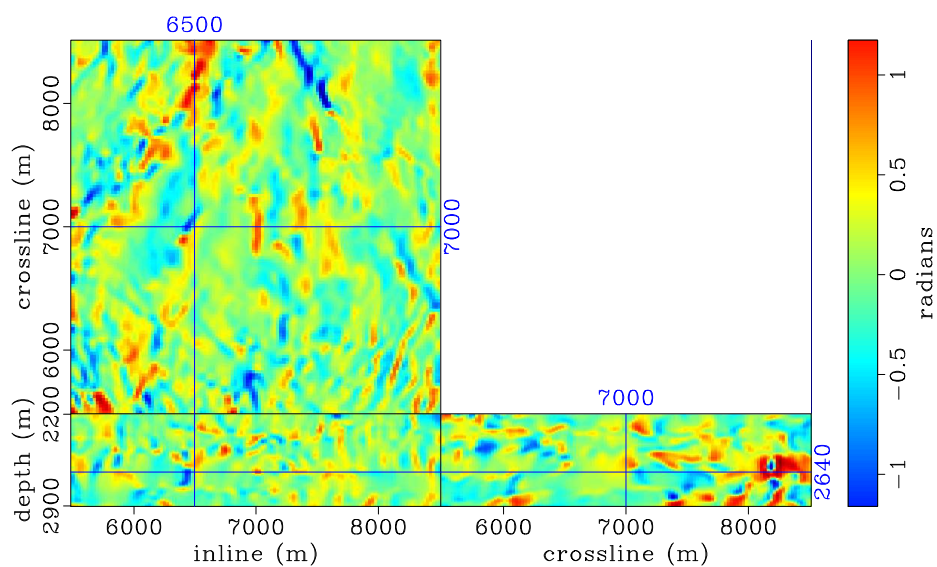
Because warping ensures that subsurface image points in the baseline and monitor images are collocated, artifacts in the initial time-lapse image (Figure 6.19) caused by misalignments due to velocity changes and compaction, have been removed in Figure 6.22(a). As discussed chapters 3, I assume that errors introduced by this kinematic correction are negligible compared to the changes in reflectivity of interest. Therefore, amplitude differences between the warped time-lapse image derived from the incomplete data sets (Figure 6.22(a)) and that from the complete data sets (Figure 6.22(b)) are due to the incomplete monitor geometry in Figure 6.22(a).

The aligned baseline and monitor images are the inputs into regularized joint image-domain inversion.

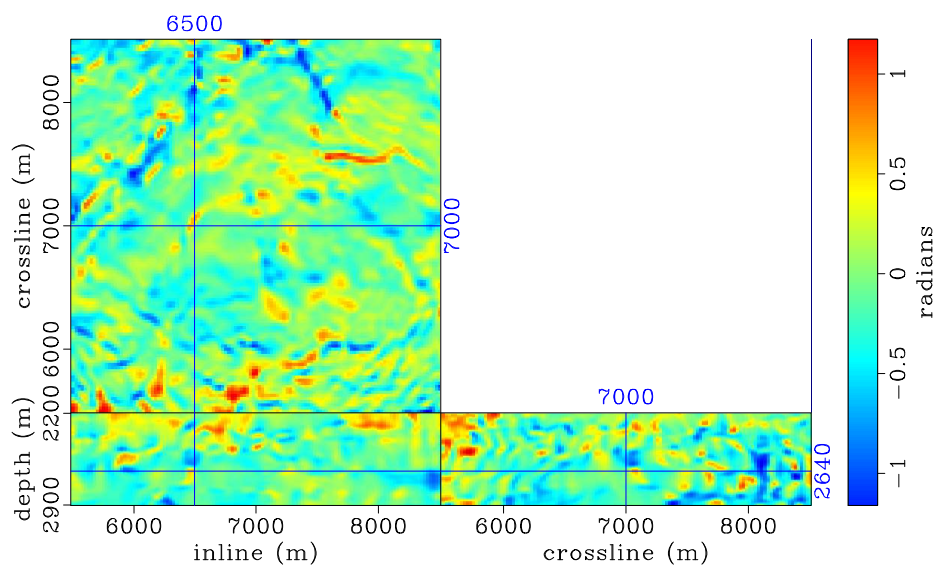
Inversion

The structure of the target-oriented Hessian matrices for the complete (baseline) and incomplete (monitor) geometries has been previously described in this section. Using these matrices, I perform regularized joint image-domain inversion for the target area. To obtain the inverted images, I perform 200 conjugate-direction iterations (Claerbout and Fomel, 2011).

As in previous chapters, I regularize the inversion spatially using factorized directional Laplacians based on dips estimated from the baseline image. Because the monitor image is aligned to the baseline image, I use the same dips to build the spatial regularization operators for both images. Figure 6.23 shows the inline and crossline dips obtained by plane-wave destruction (Fomel, 2002). In this example (and in other inversion results in this chapter), I use the full factorized three-dimensional dip filters, which are constructed as described in chapter 3. As in previous examples, the tem-



(a)



(b)

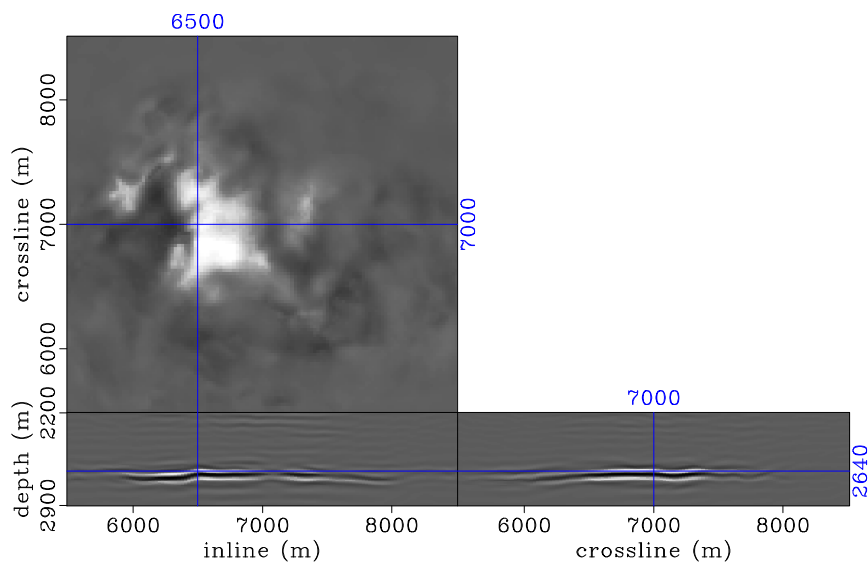
Figure 6.23: Inline (a) and crossline (b) dips estimated from the baseline image (Figure 6.18(a)) using the plane-wave destruction method (see Fomel (2002)). These dips are used to construct the spatial regularization operator for the inversion. [CR] chap6/. dip-x,dip-y

poral regularization is a difference operator between the baseline and monitor images. This temporal regularization operator provides coupling between the inverted baseline and monitor images and ensures that there are only limited differences between them.

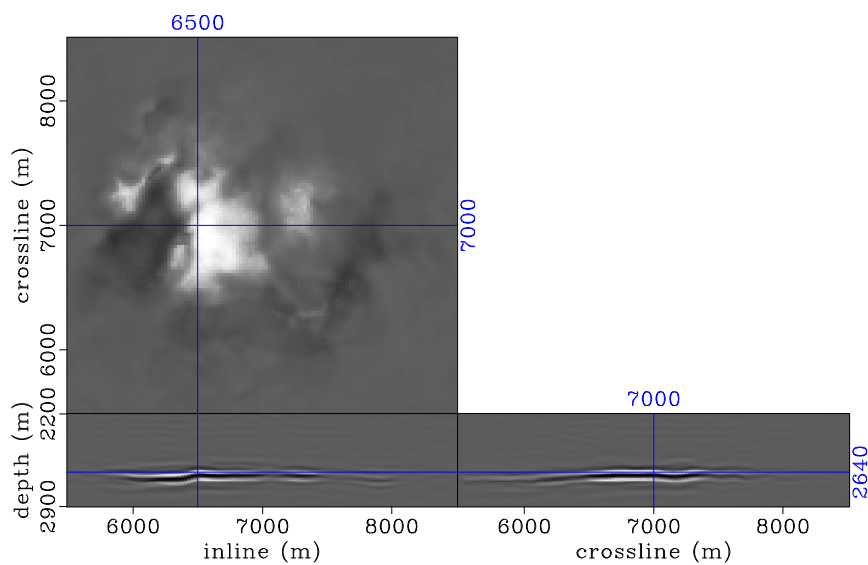
The time-lapse image of the target area obtained by regularized joint image-domain inversion of the complete baseline and incomplete monitor data sets is presented in Figure 6.24(a). For comparison, the time-lapse image obtained from inversion of the complete baseline and complete monitor data sets is presented in Figure 6.24(b). As shown in Figure 6.24, the inverted time-lapse images obtained in both cases are relatively similar, compared to those obtained from migration (Figure 6.22). Importantly, note that the inverted time-lapse image derived from the complete baseline and incomplete monitor data (Figure 6.24(a)) contain fewer obstruction artifacts, compared to those in the migrated time-lapse image derived from the same data (Figure 6.22(a)). In addition, the inverted time-lapse images (Figure 6.24) have better resolution than the migrated time-lapse images (Figure 6.22).

The inverted baseline and monitor images, from which the time-lapse image in Figure 6.24(a) is computed, are presented in Figure 6.25. A comparison of these inverted images with the migrated baseline and monitor images (Figures 6.18) shows that inversion provides reflectivity images with better resolution and more balanced amplitudes than migration.

To study the improvements provided by regularized joint image-domain inversion, I compute the average time-lapse amplitudes within a 60 m window around the reservoir. I obtain these amplitudes by computing difference between the average absolute amplitudes in the baseline and monitor images. The time-lapse amplitudes obtained by migration and by inversion are presented in Figure 6.26. Figures 6.26(a) and 6.26(b) are the migrated time-lapse amplitude maps from the incomplete and complete data sets, respectively. The corresponding time-lapse amplitude maps, from the incomplete and complete data are presented in Figures 6.26(c) and 6.26(d), respectively. A comparison of these amplitude maps shows that, whereas the results from the migrated images differ significantly, those obtained from inversion are similar.

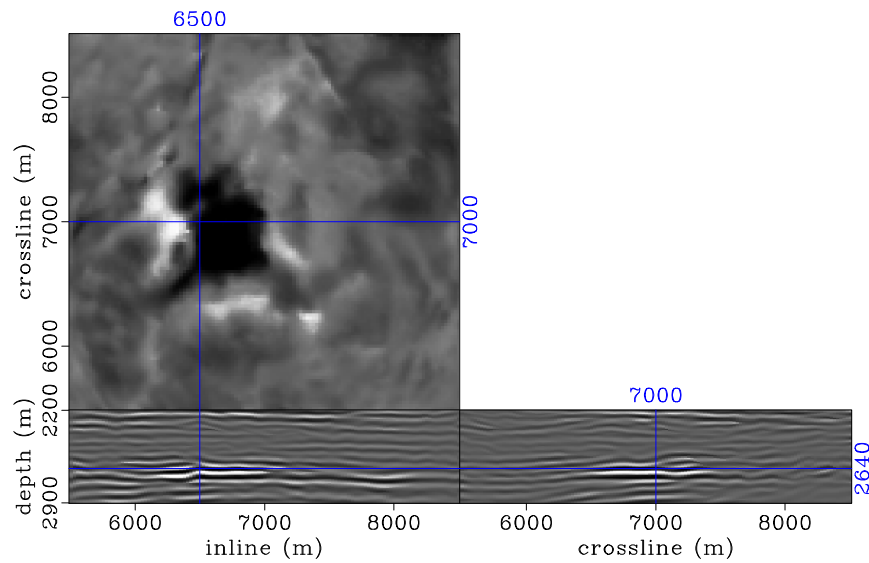


(a)

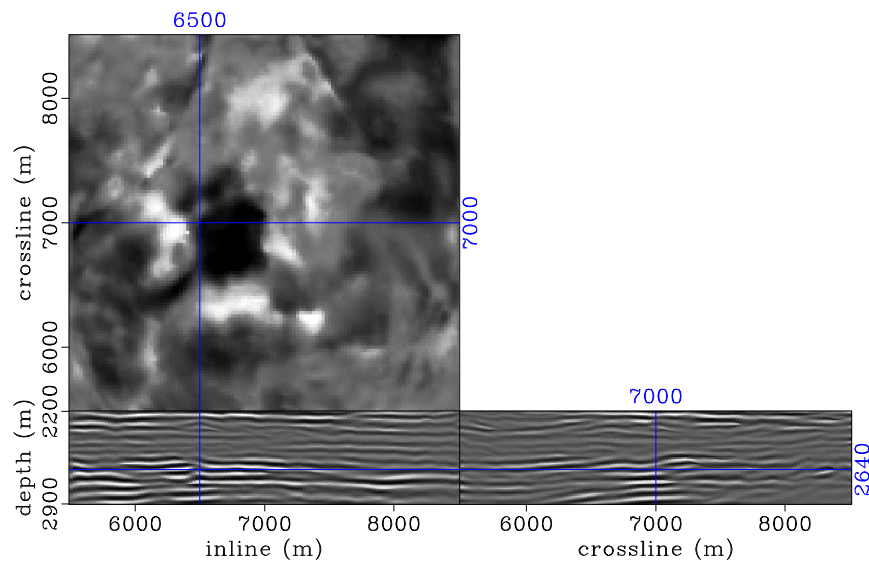


(b)

Figure 6.24: Time-lapse images of the target area obtained from regularized image-domain inversion of the incomplete (a) and complete (b) data sets. Note that these inverted time-lapse images are comparable. In (a), obstruction artifacts in the migrated time-lapse image (Figure 6.22(a)) have been attenuated by inversion. In addition, this inverted time-lapse image shows improved resolution over the migrated time-lapse image. A comparison of the time-lapse amplitudes along the reservoir is presented in Figure 6.26. [CR] chap6/. gap-d-inv, fine-d-inv



(a)



(b)

Figure 6.25: Inverted baseline image (a), and monitor image (b) of the target area obtained from the complete baseline and incomplete monitor data sets. The difference between these images, which are obtained by regularized joint image-domain inversion, is presented in Figure 6.24(a). Compared to the migrated images in Figure 6.18, these images show improved resolution of the subsurface reflectivity. [CR]

chap6/. gap-1,gap-2

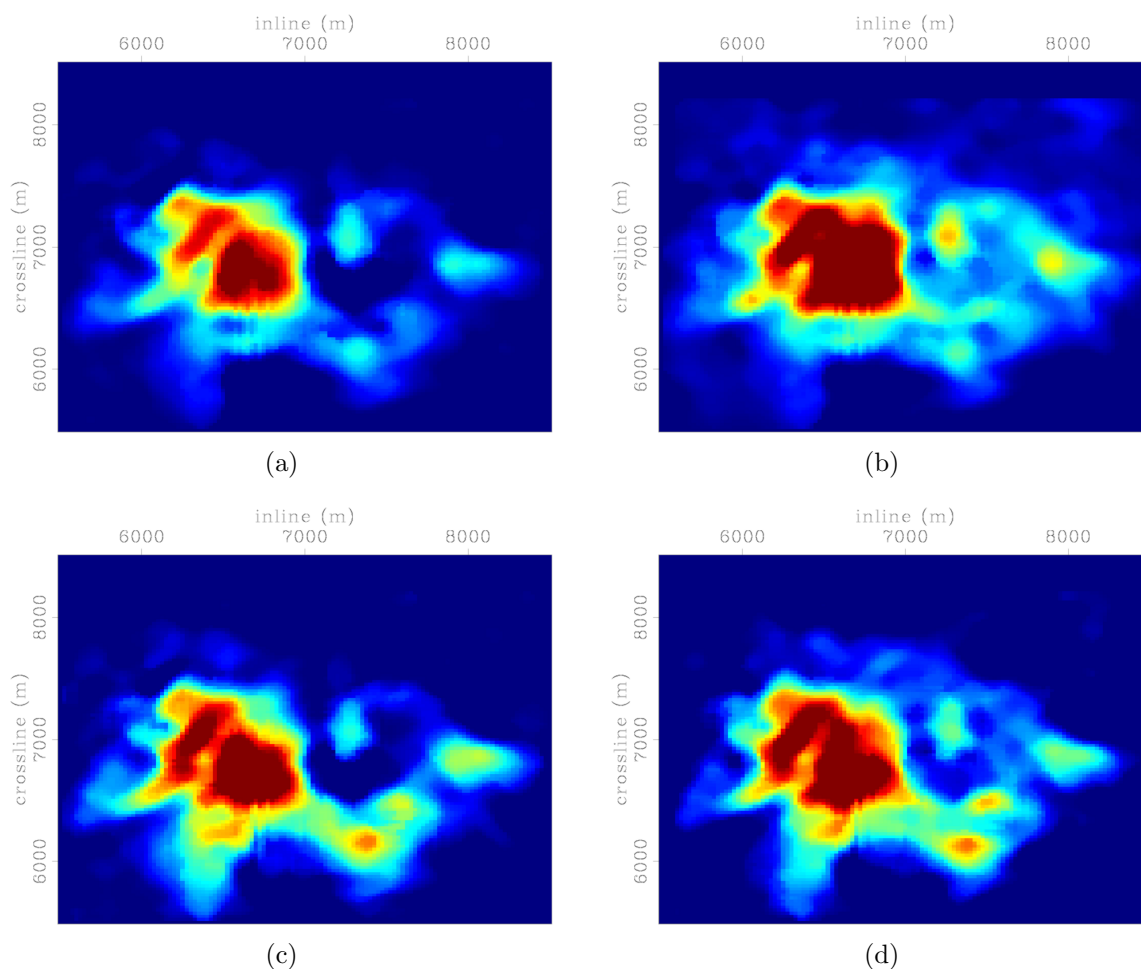


Figure 6.26: Average time-lapse amplitudes within a 60 m window around the reservoir obtained from migration (a) and (b), and from regularized image-domain inversion (c) and (d). Figures (a) and (c) are the reference amplitudes obtained from the complete data, whereas (b) and (d) are obtained from the incomplete data. These amplitude maps are presented at the same clip level relative to the respective baseline and monitor images. Note the discrepancies in the time-lapse amplitude distribution obtained via migration of the complete (a), and incomplete (b) data. This discrepancy has been attenuated via inversion of the same data sets (c) and (d). [CR]

chap6/. hor-4-d3,hor-4-d2,hor-4-d1,hor-4-d

Example II: Inversion of multiple data sets

In this section, using data from the first (LoFS 1), the fifth (LoFS 5), and the ninth (LoFS 9) surveys, I demonstrate an application of joint image-domain inversion to multiple data sets. In this example, LoFS 1 is the baseline survey, LoFS 5 is the first monitor survey, and LoFS 9 is the second monitor survey. As described in example *I*, LoFS 1 and LoFS 9 were acquired in November 2003 and December 2007, respectively. LoFS 5 data set, which was acquired in April 2005, has been preprocessed by the donor using the same parameters as in LoFS 1 and LoFS 9.

In this example, the geometry of the baseline survey is the same as that in example *I*. Furthermore, the geometry of the second monitor survey is the same as the that of the incomplete monitor survey in example *I*. However, to simulate a different geometry for the first monitor survey in this example, I create 1.44 km² gap in the source geometry and a 1.0 km² gap in the receiver geometry (Figure 6.27). Because of the different sizes of gaps in the geometries of the two monitor surveys, the three surveys in this example have different acquisition geometries.

Using the same parameters as in Example *I*, I compute the diagonal of the Hessian matrices (i.e., the subsurface illumination) corresponding to the three geometries. Figure 6.28 shows the subsurface illumination ratio between the incomplete geometry of the first monitor survey and the complete baseline survey. Recall that in example *I*, the illumination ratio between the incomplete geometry of the second monitor survey and the complete baseline survey was discussed (Figure 6.11(b)). To provide a measure of the differences in illumination along the reservoir that are caused by the differences in survey geometries, I compute the average illumination ratio within a 60 m window around the reservoir. Figures 6.29(a) and 6.29(b) show maps of the illumination ratio between the baseline and the first monitor, and between the baseline and the second monitor, respectively.

I migrate the baseline and monitor data sets using the same parameters as in example *I*. Prior to inversion, as in previous examples, I warp the two monitor images to the baseline using the sequential warping method described in chapter 2.

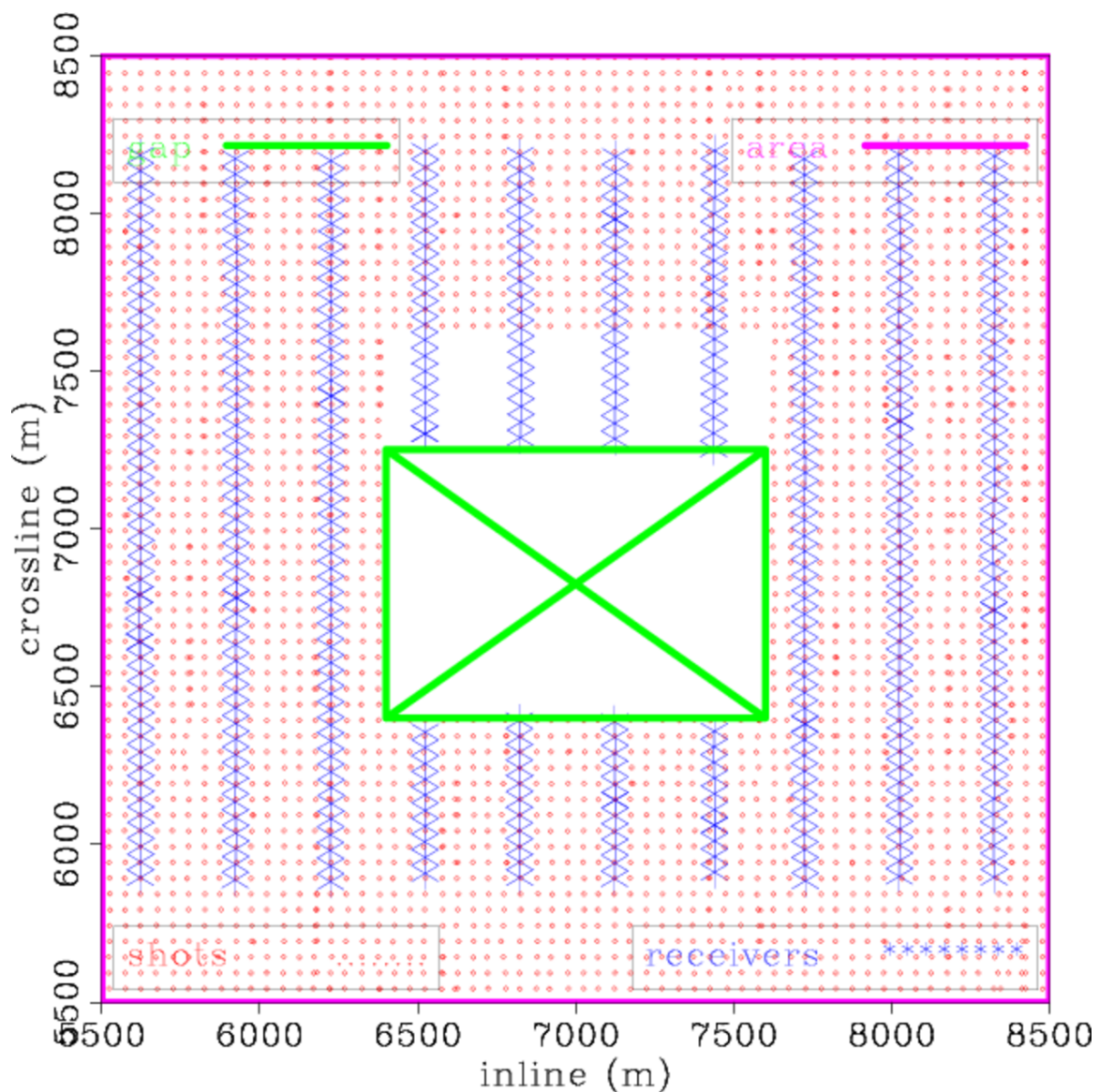


Figure 6.27: An enlarged view of the study area (Figure 6.3) showing the shot and receiver locations within the study area, and the location of the simulated obstruction in the geometry the first monitor (LoFS 5). Note that the gap in the source locations is bigger than the gap in the receiver locations. There are not sources and receivers within the overlap area. Compare this to Figures 6.4 and 6.6, which show the complete baseline geometry and the incomplete geometry of the second monitor.

[ER] chap6/. OOsfull-5-gap

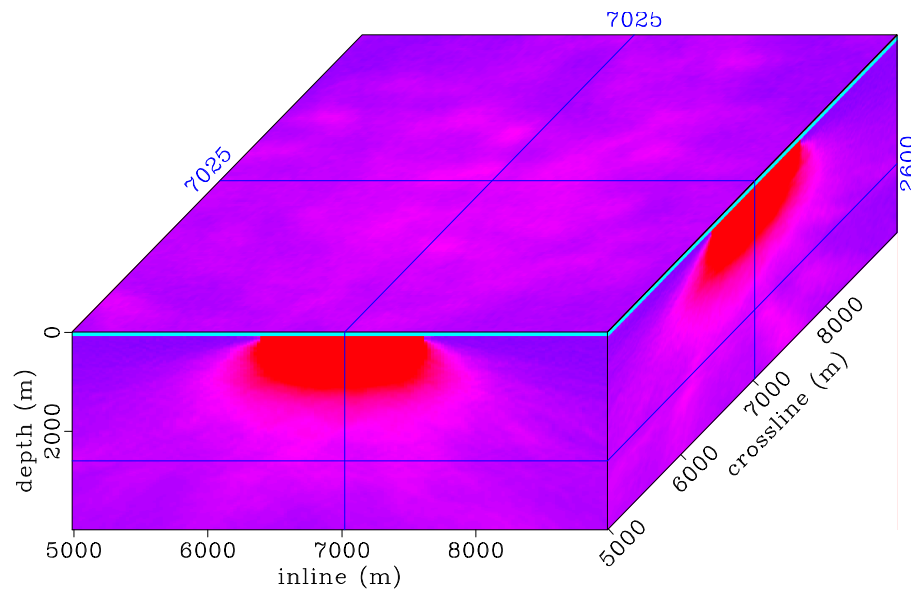


Figure 6.28: Subsurface illumination ratio between the complete baseline survey and the incomplete *first* monitor survey, showing a depth slice through the reservoir. Compare this figure to the illumination ratio between the baseline and the second monitor survey (Figure 6.11(b)). The illumination ratio between the baseline and the two monitor geometries along the reservoir are shown in Figure 6.29. [CR] chap6/. ilumr1-4

For comparison, I apply the same procedure and parameters to the complete baseline and monitor data sets. The time-lapse amplitudes along the reservoir, obtained from the warped migrated images, are presented in Figure 6.30. As shown in Figure 6.30, there are large discrepancies in the time-lapse amplitudes obtained from migration of the complete data and those from the incomplete data.

The inverted reservoir time-lapse amplitude maps are presented in Figure 6.31. A comparison of the inverted maps from the complete data (Figures 6.31(a) and 6.31(c)) and the incomplete data (Figures 6.31(b) and 6.31(d)) show that, compared to the migrated amplitude maps (Figure 6.30), regularized joint image-domain inversion minimizes the discrepancies in time-lapse amplitude information caused by geometry differences between surveys. However, a comparison of Figures 6.31(a) and 6.31(b) shows that this method is not perfect. In particular, where the reflectivity changes are small and the geometry differences are large, although regularized joint inversion

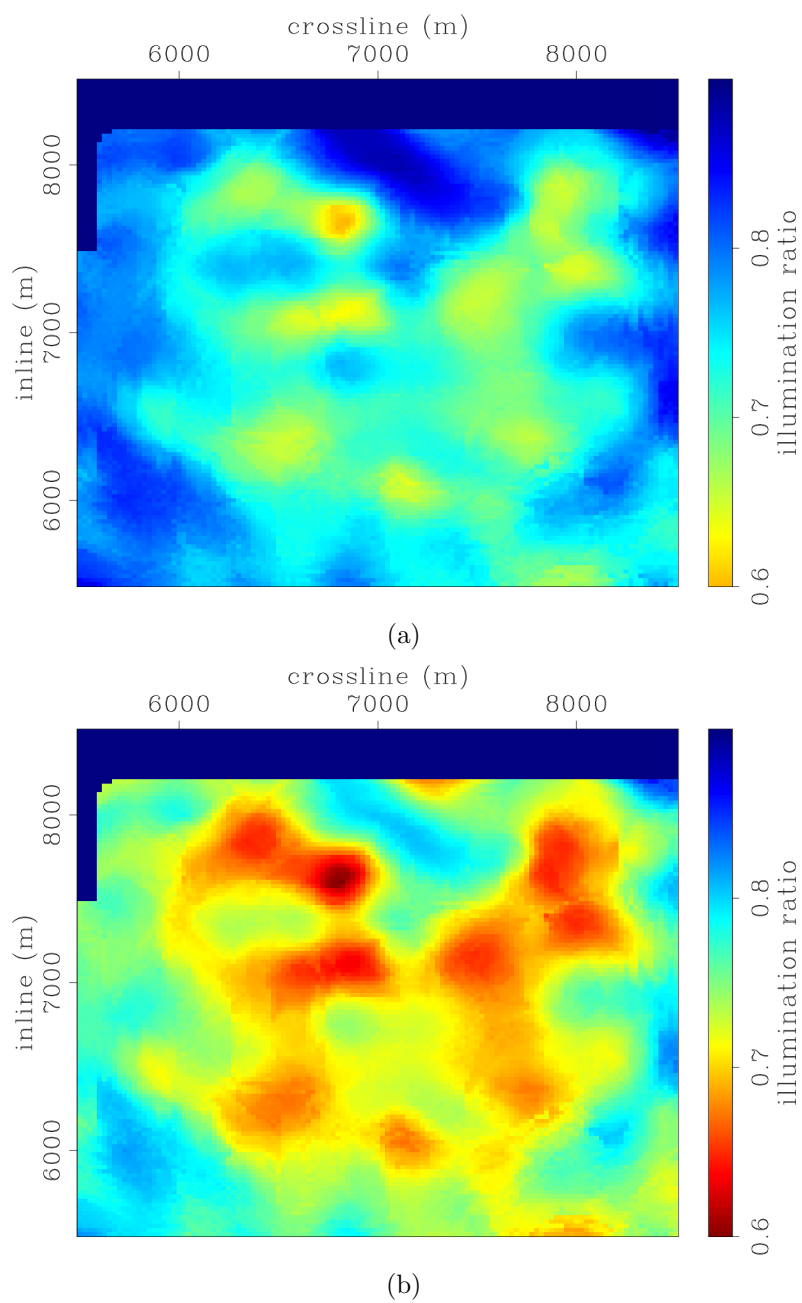


Figure 6.29: Illumination ratio between the baseline and the first monitor (a), and between the baseline and the second monitor (b). In these maps, red indicates regions with the largest illumination disparity, whereas blue indicates regions with the smallest illumination disparity. In both examples, although the geometry difference is caused by a rectangular gap in the monitor geometries, the illumination disparities are complex at depth. [CR] chap6/. ilum-res-1r,illum-res-2r

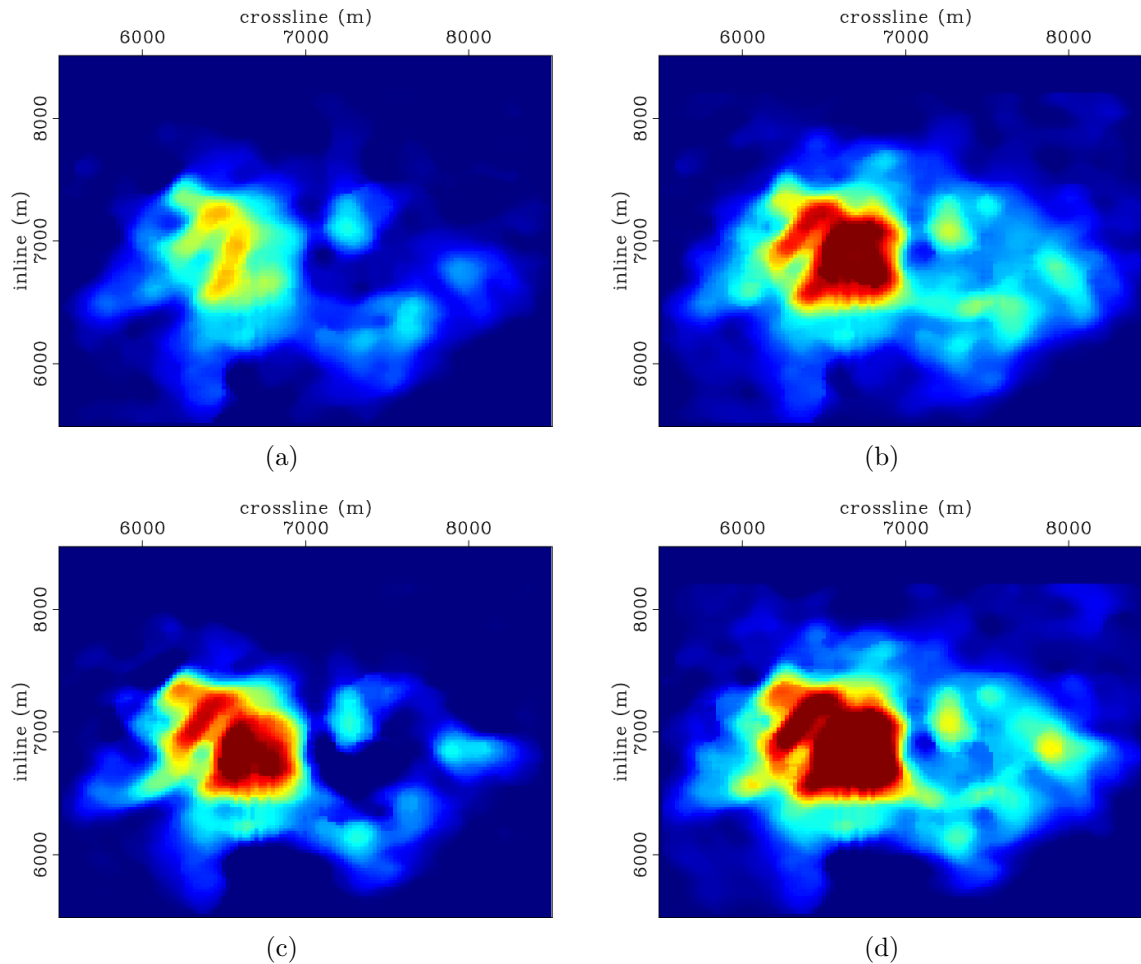


Figure 6.30: Average time-lapse amplitudes within a 60 m window around the reservoir obtained from migration. Panels (a) and (c) are the difference maps between the complete baseline, and the complete first and second monitor, respectively. Panels (b) and (d) are the corresponding results from the complete baseline and the incomplete monitor data. These amplitude maps are presented at the same clip relative to the respective baseline and monitor images. Note that there are large discrepancies in the time-lapse amplitude distribution obtained via migration of the complete and incomplete data sets. [CR]

chap6/. h3-fine-mod-dd1,h3-gap-mod-dd1,h3-fine-mod-dd2,h3-gap-mod-dd2

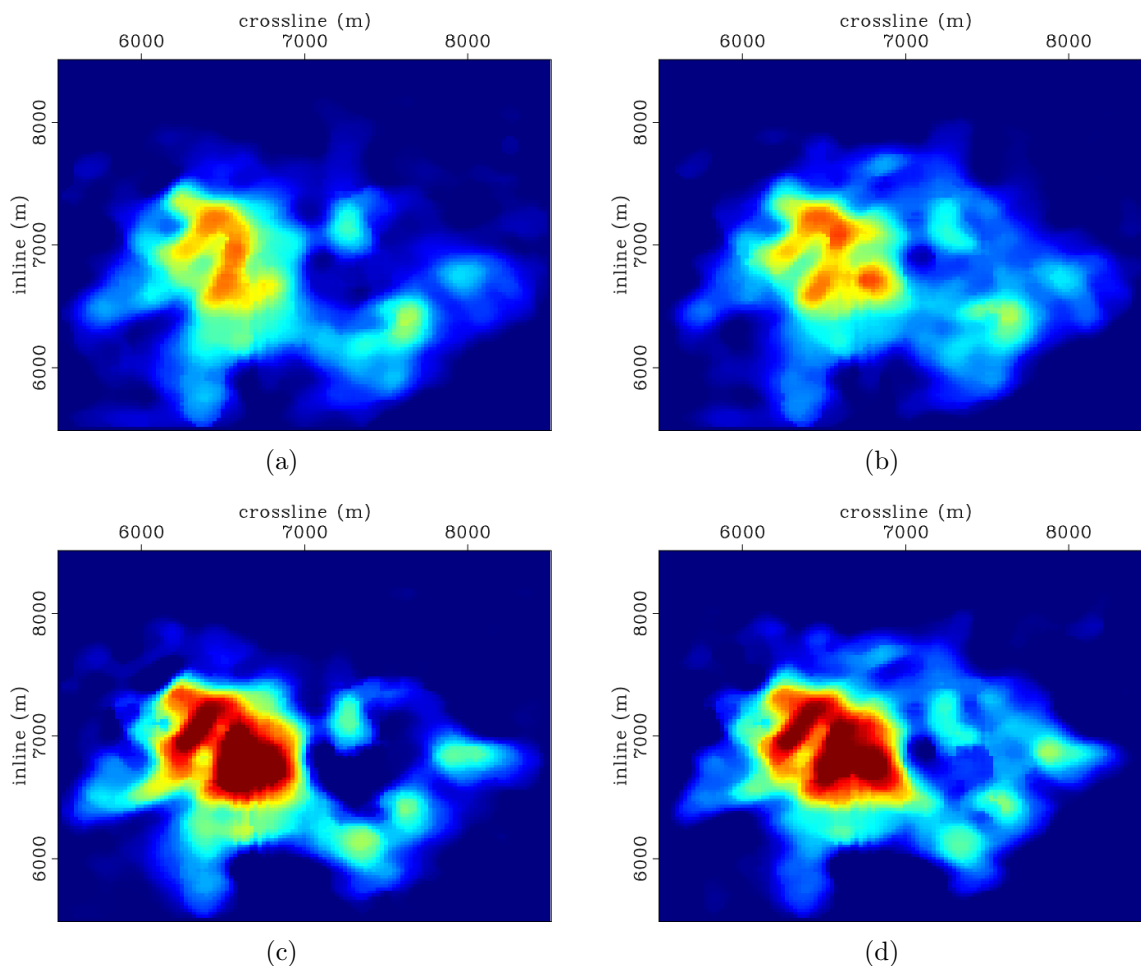


Figure 6.31: Average time-lapse amplitudes within a 60 m window around the reservoir obtained from regularized joint image-domain inversion. Panels (a) and (c) are the difference maps between the complete baseline, and the complete first and second monitor, respectively. Panels (b) and (d) are the corresponding results from the complete baseline and the incomplete monitor data. These amplitude maps are presented at the same clip relative to the respective baseline and monitor images. Note that discrepancies in the time-lapse amplitude distribution in the migrated results (Figure 6.30) have been reduced. [CR]

chap6/. h3-fine-dd1,h3-gap-dd1,h3-fine-dd2,h3-gap-dd2

will provides more reliable results than migration, it will not fully recover the true reflectivity change.

Example III: Multiple realizations of time-lapse images

In this section, I demonstrate how multiple plausible realizations of the time-lapse image can be obtained from regularized inversion. As noted in chapter 3, one advantage of image-domain inversion is that it allows the linearized inversion problem to be solved in a target-oriented manner. This reduces the size of the computational domain and hence the inversion cost. In addition, as described in previous chapters, each iteration of image-domain inversion requires matrix-vector multiplications, instead of migration and demigration operations required in each iteration of data-domain inversion. Therefore, once the Hessian matrices are computed, regularized joint image-domain inversion is computationally inexpensive, and it is possible to test different constraints in the inversion very rapidly.

Here, I examine how the temporal regularization parameter affects the estimated time-lapse amplitudes. The premise is that, depending on the data quality and the strength of the time-lapse seismic signal, the baseline and monitor images should be similar at most subsurface image positions. The task then is to determine how similar or how different the baseline and monitor images should be. One way to accomplish this is through matched filtering, based on filters derived from non-reservoir parts of the subsurface images. However, as described in chapter 2, matched filtering suffers from several pitfalls. Regularized inversion provides a way to achieve this same requirement by utilizing available information about the subsurface reservoir and expected changes as constraints in the inversion.

In this example, I consider the complete baseline data (LoFS 1), and complete monitor data (LoFS 9). Recall that the geometry of these data sets, along with the preprocessing and migration parameters, and the spatial and temporal regularization operators used in the inversion are described in example *I*.

Figure 6.32 shows the image-fitting residuals as a function of the iteration number, which are obtained with six different regularization parameters. Each curve is scaled by the maximum fitting residual—at the first iteration. As expected, this plot shows that the minimum image-fitting residual increases as a function of the temporal coupling between the images. In general, a high temporal coupling means that the differences between the baseline and monitor images are constrained to be small, whereas a small temporal coupling means that large differences are allowed between the baseline and monitor images. The inverted reservoir time-lapse amplitude maps that correspond to these graphs are presented in Figure 6.33.

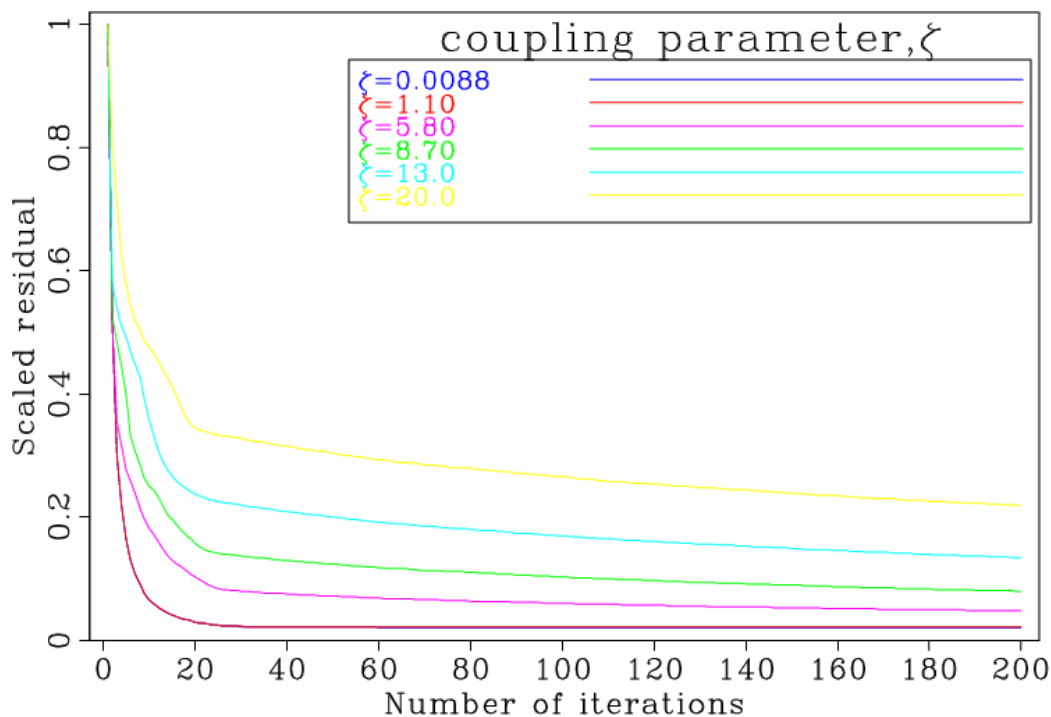


Figure 6.32: Scaled residual for six different regularization parameters. Each graph corresponds to a different temporal regularization parameter, expressed as a percentage of the RMS energy in the migrated baseline image. All the graphs are obtained with the same spatial regularization parameter but different temporal constraints. As expected, large temporal constraints lead to higher residuals. These graphs correspond to the residuals for the amplitude maps in Figure 6.33. [CR]. chap6/. mult-rd

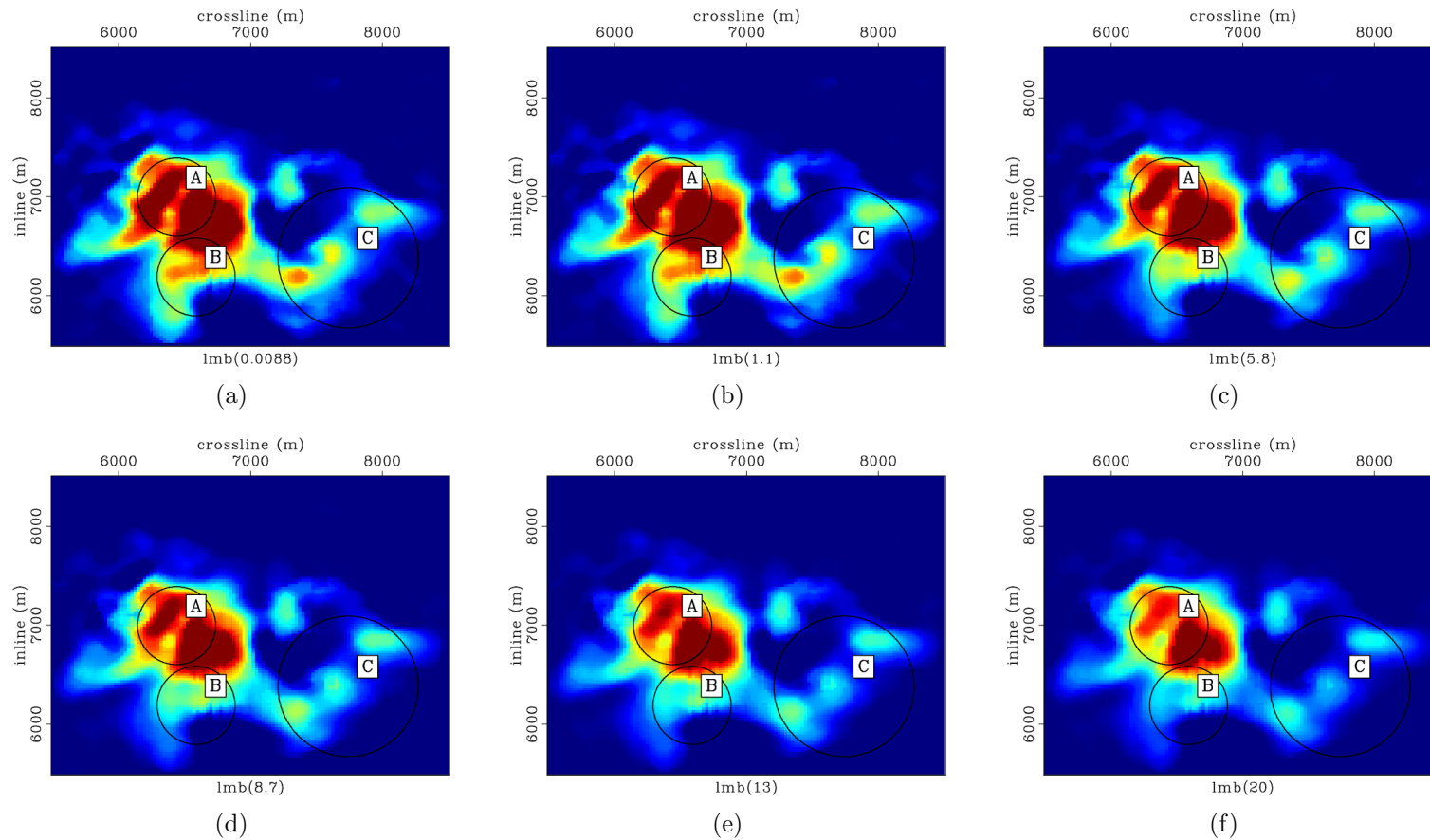


Figure 6.33: Average time-lapse amplitudes within a 60 m window around the reservoir obtained from using different regularization parameters in the image-domain inversion of the complete baseline and monitor data. In these maps, which are presented at the same clip relative to the baseline and monitor images, the temporal (coupling) regularization parameter increases from (a) to (f). These amplitude maps are obtained with the same spatial regularization parameter. Especially within the ovals (labeled A, B and C), note the systematic changes in the time-lapse amplitudes as a function of the coupling strength. [CR] chap6/. mult-1,mult-2,mult-3,mult-4,mult-5,mult-6

As shown in Figure 6.33, there is a systematic change in the reservoir time-lapse amplitudes as a function of the temporal coupling between the baseline and monitor images. In particular, there are significant differences in the time-lapse amplitude map within the ovals (labeled A, B and C). For example, there is a feature in the time-lapse amplitude map within oval B when the temporal coupling is small (e.g., Figure 6.33(a)). This feature disappears as at high temporal coupling (e.g., Figure 6.33(f)).

DISCUSSION AND CONCLUSIONS

A common problem in many time-lapse seismic monitoring surveys is the presence of obstructions that create gaps in the monitor data. Such obstructions, usually caused by production and drilling facilities, generate artifacts that contaminate production-related seismic amplitudes changes, thereby limiting our ability to accurately interpret observed time-lapse amplitudes. The Valhall LoFS project provides data with high repeatability of both source and receiver locations (Figures 6.2 to ??). Therefore, in this case study, the major sources of time-lapse amplitude contamination are the synthesized gaps in the monitor data. Example *I* shows clearly how inversion can be used to attenuate these contaminating artifacts.

Surface (CMP) folds only provide limited information about geometry differences between surveys (Figure 6.7). Importantly, because surface folds do not provide information about the effects of such geometry differences in the subsurface, information derived from them cannot be used to compensate for the associated subsurface illumination differences. As shown in Figures 6.8 to 6.10, the diagonal of the Hessian matrix provides a good measure of the subsurface illumination for any given geometry. An estimate of the subsurface illumination differences can be obtained from the ratio of the Hessian matrices for the different survey geometries (Figure 6.11).

Although the diagonal of the Hessian matrix provides important information about subsurface illumination and differences, the band-limited wave-propagation effects are provided by the off-diagonals elements of the matrix (Figure 6.12). it is

common practice to correct for subsurface illumination using weights derived from the inverse of the diagonal of the Hessian matrix. However, this approximation assumes that at any subsurface image point, all wavenumbers/dips are illuminated equally. Instead of such approximation, the truncated target-oriented Hessian captures the dip-dependent subsurface illumination (Figure 6.13). Importantly, where time-lapse surveys have different geometries, at any subsurface image point, there are differences in the illumination of different wavenumbers (Figure 6.13(b)). Therefore, as shown in Figure 6.13, the off-diagonal elements of the Hessian matrices provide the information necessary to correctly account for such geometry differences.

An important assumption in the joint inversion method developed in this dissertation is that the velocity is nearly accurate. For this study, the velocity model obtained via full-waveform inversion—and used in several previous studies—satisfies this requirement. As shown in Figures 6.14 to 6.17, using this velocity model, all the key geological horizons in the study area are well imaged. In addition, because the inversion problem is posed in the image domain, I perform inversion only for a small target area around the reservoir (Figures 6.14 to 6.17). Because the target area is small, it is possible to focus efforts to improve results in the region where the most important production- or injection-related changes are expected.

As previously described in this dissertation, prior to inversion, the monitor image is aligned to the baseline image. This multidimensional image alignment is performed efficiently by warping the two images using apparent displacements derived from a one-dimensional sequential warping (Figures 6.20 and 6.21). These apparent displacements are due to a combined effect of deformation and velocity changes associated with hydrocarbon production and water injection in the study area.

Conventional imaging by migration does not account for the geometry differences between the data sets. Because it attenuates artifacts caused by geometry differences between the baseline and monitor images (Figure 6.22(a)), regularized joint image-domain inversion provides time-lapse images with improved quality and more reliable amplitudes (Figure 6.24(a)) compared to migration (Figure 6.22(a)). In addition, because joint inversion accounts for band-limited wave-propagation effects, it provides

subsurface images with improved resolution. Therefore, inverted time-lapse images show improved resolution compared to the migrated time-lapse images (Figure 6.22(a) versus Figure 6.22(a)).

In example *I*, because of the geometry differences between the baseline and monitor surveys, there is a large disparity in the distribution of time-lapse amplitudes for the complete (Figures 6.26(a)) and incomplete (Figure 6.26(b)) data sets. Regularized joint image-domain inversion corrects for this disparity, thereby providing comparable time-lapse amplitude distributions in both the complete and incomplete data examples (Figures 6.26(c) and 6.26(d)).

The regularized joint inversion formulations developed in this dissertation can be applied to any number of surveys. As shown in example *II*, when applied to data sets from three surveys using similar and different geometries, inversion provides more reliable time-lapse amplitude information than does migration. Where multiple surveys have dissimilar geometries, there can be strong dissimilarities in the reservoir illumination (Figure 6.29). These dissimilarities between surveys will affect the reservoir time-lapse amplitudes in different ways (Figure 6.30). Regularized joint inversion provides a framework to account for these differences in an integrated manner, thereby providing more reliable time-lapse amplitude information (Figure 6.31).

From the results in examples *I* and *II*, it is clear that the inverted time-lapse amplitudes derived from the complete data sets and those from the incomplete data are similar. Therefore, I conclude that the regularized joint image-domain inversion method developed in this dissertation can reduce the sensitivity of the time-lapse seismic amplitudes to differences in acquisition geometries.

As discussed in this and in previous chapters, once the approximate Hessian matrices are computed, regularized image-domain inversion is computationally inexpensive. This, combined with the fact that it readily permits inversion of a small target around the reservoir, makes it possible to efficiently test different combinations of regularization parameters. In example *III*, by using different realistic coupling parameters (Figure 6.32), I obtain six possible inverted time-lapse images (Figure 6.33). All these

results, obtained using 200 conjugate iterations, are derived in less than 1 hour on 553 CPU cores. Therefore, depending on the available computer resources, one can quickly test a wide range of realistic constraints in the inversion.

Because regularized joint image-domain inversion is based on the physics of the seismic data acquisition and imaging, it provides a robust way to enforce similarity between the baseline and monitor images without damaging the time-lapse amplitudes of interest. As shown in Figure 6.33, the inverted reservoir time-lapse amplitudes depend on the temporal coupling between the baseline and monitor images. Although not included in this study, the time-lapse amplitudes will also vary as a function of the spatial regularization parameter. By studying the characteristics of the estimated time-lapse amplitudes, and comparing these with other available data, an interpreter can make informed decisions on the time-lapse amplitudes. For example, these results can be used to quantify uncertainties associated with the observed time-lapse amplitude changes. In addition, because any one time-lapse image may not match other geological or engineering data, these multiple realizations can be used as part of an integrated production history matching.

ACKNOWLEDGMENTS

I thank BP and Valhall partners for donating the time-lapse data sets used in this chapter. In particular, I thank Adeyemi Arogumati and Olav Barkved (both of BP) for their assistance. I thank the Stanford Center for Computational Earth and Environmental Science (CEES) for providing the computer resources used in these studies.